



LJMU Research Online

Wilson, S, Hilton, M, Rooney, PJ, Caldwell, CE, Kay, ST, Collins, CA, McCarthy, IG, Romer, AK, Bermeo-Hernandez, A, Bernstein, R, Costa, LD, Gifford, D, Hollowood, D, Hoyle, B, Jeltema, T, Liddle, AR, Maia, MAG, Mann, RG, Mayers, JA, Mehrtens, N, Miller, CJ, Nichol, RC, Ogando, R, Sahlén, M, Stahl, B, Stott, JP, Thomas, PA, Viana, PTP and Wilcox, H

The XMM Cluster Survey: evolution of the velocity dispersion -- temperature relation over half a Hubble time

<http://researchonline.ljmu.ac.uk/id/eprint/2525/>

Article

Citation (please note it is advisable to refer to the publisher's version if you intend to cite from this work)

Wilson, S, Hilton, M, Rooney, PJ, Caldwell, CE, Kay, ST, Collins, CA, McCarthy, IG, Romer, AK, Bermeo-Hernandez, A, Bernstein, R, Costa, LD, Gifford, D, Hollowood, D, Hoyle, B, Jeltema, T, Liddle, AR, Maia, MAG, Mann, RG, Mayers, JA, Mehrtens, N, Miller, CJ, Nichol, RC, Ogando, R, Sahlén, M.

LJMU has developed **LJMU Research Online** for users to access the research output of the University more effectively. Copyright © and Moral Rights for the papers on this site are retained by the individual authors and/or other copyright owners. Users may download and/or print one copy of any article(s) in LJMU Research Online to facilitate their private study or for non-commercial research. You may not engage in further distribution of the material or use it for any profit-making activities or any commercial gain.

The version presented here may differ from the published version or from the version of the record. Please see the repository URL above for details on accessing the published version and note that access may require a subscription.

<http://researchonline.ljmu.ac.uk/>

For more information please contact researchonline@ljmu.ac.uk

<http://researchonline.ljmu.ac.uk/>

The *XMM* Cluster Survey: evolution of the velocity dispersion–temperature relation over half a Hubble time

Susan Wilson,^{1★} Matt Hilton,^{1★} Philip J. Rooney,² Caroline Caldwell,³ Scott T. Kay,⁴ Chris A. Collins,³ Ian G. McCarthy,³ A. Kathy Romer,² Alberto Bermeo,² Rebecca Bernstein,⁵ Luiz da Costa,^{6,7} Daniel Gifford,⁸ Devon Hollowood,⁹ Ben Hoyle,¹⁰ Tesla Jeltema,⁹ Andrew R. Liddle,¹¹ Marcio A. G Maia,^{6,7} Robert G. Mann,¹¹ Julian A. Mayers,³ Nicola Mehrrens,^{12,13} Christopher J. Miller,⁸ Robert C. Nichol,¹⁴ Ricardo Ogando,^{6,7} Martin Sahlén,¹⁵ Benjamin Stahl,⁹ John P. Stott,¹⁶ Peter A. Thomas,² Pedro T. P. Viana^{17,18} and Harry Wilcox¹⁴

¹*Astrophysics and Cosmology Research Unit, School of Mathematics, Statistics and Computer Science, University of KwaZulu-Natal, Durban 4041, South Africa*

²*Astronomy Centre, University of Sussex, Falmer, Brighton BN1 9QH, UK*

³*Astrophysics Research Institute, Liverpool John Moores University, IC2, Liverpool Science Park, 146 Brownlow Hill, Liverpool L3 5RF, UK*

⁴*Jodrell Bank Centre for Astrophysics, School of Physics and Astronomy, The University of Manchester, Manchester M13 9PL, UK*

⁵*Observatories of the Carnegie Institution for Science, 813 Santa Barbara Street, Pasadena, CA 91101, USA*

⁶*Observatório Nacional, Rua Gal. José Cristino 77, Rio de Janeiro RJ - 22460-040, Brazil*

⁷*Laboratório Interinstitucional de e-Astronomia - LIneA, Rua Gal. José Cristino 77, Rio de Janeiro RJ - 20921-400, Brazil*

⁸*Astronomy Department, University of Michigan, Ann Arbor, MI 48109, USA*

⁹*Department of Physics and Santa Cruz Institute for Particle Physics, University of California, Santa Cruz, CA 95064, USA*

¹⁰*Universitäts-Sternwarte, Fakultät fuer Physik, Ludwig-Maximilians Universität Muenchen, Scheinerstr. 1, D-81679 Muenchen, Germany*

¹¹*Institute for Astronomy, University of Edinburgh, Royal Observatory, Blackford Hill, Edinburgh EH9 3HJ, UK*

¹²*George P. and Cynthia Woods Mitchell Institute for Fundamental Physics and Astronomy, Texas A & M University, College Station, TX 77843-4242, USA*

¹³*Department of Physics and Astronomy, Texas A & M University, College Station, TX 77843-4242, USA*

¹⁴*Institute of Cosmology and Gravitation, University of Portsmouth, Dennis Sciama Building, Portsmouth PO1 3FX, UK*

¹⁵*BIPAC, Department of Physics, University of Oxford, Denys Wilkinson Building, 1 Keble Road, Oxford OX1 3RH, UK*

¹⁶*Sub-department of Astrophysics, Department of Physics, University of Oxford, Denys Wilkinson Building, Keble Road, Oxford OX1 3RH, UK*

¹⁷*Instituto de Astrofísica e Ciências do Espaço, Universidade do Porto, CAUP, Rua das Estrelas, P-4150-762 Porto, Portugal*

¹⁸*Departamento de Física e Astronomia, Faculdade de Ciências, Universidade do Porto, Rua do Campo Alegre, 687, P-4169-007 Porto, Portugal*

Accepted 2016 August 3. Received 2016 July 26; in original form 2015 December 3

ABSTRACT

We measure the evolution of the velocity dispersion–temperature (σ_v – T_X) relation up to $z = 1$ using a sample of 38 galaxy clusters drawn from the *XMM* Cluster Survey. This work improves upon previous studies by the use of a homogeneous cluster sample and in terms of the number of high-redshift clusters included. We present here new redshift and velocity dispersion measurements for 12 $z > 0.5$ clusters observed with the Gemini Multi Object Spectrographs instruments on the Gemini telescopes. Using an orthogonal regression method, we find that the slope of the relation is steeper than that expected if clusters were self-similar, and that the evolution of the normalization is slightly negative, but not significantly different from zero ($\sigma_v \propto T^{0.86 \pm 0.14} E(z)^{-0.37 \pm 0.33}$). We verify our results by applying our methods to cosmological hydrodynamical simulations. The lack of evolution seen in our data is consistent with simulations that include both feedback and radiative cooling.

Key words: galaxies: clusters: general – galaxies: clusters: intracluster medium – galaxies: distances and redshifts – cosmology: miscellaneous – X-rays: galaxies: clusters.

* E-mail: sWilson072@gmail.com (SW); hiltonm@ukzn.ac.za (MH)

1 INTRODUCTION

Clusters of galaxies are the largest coherent gravitationally bound objects in our Universe. By studying galaxy clusters, information can be gained about the formation of galaxies, and the effect of ongoing processes such as merging and AGN feedback. They can also be used as a probe of cosmology by studying the evolution of their number density with mass and redshift (e.g. Vikhlinin et al. 2009; Hasselfield et al. 2013; Reichardt et al. 2013; Planck Collaboration XXIV 2015). However, the mass of galaxy clusters is not a quantity that can be directly measured, and therefore it needs to be determined using observable mass tracers such as X-ray properties (e.g. luminosity and temperature), the Sunyaev-Zel'dovich (SZ) effect signal, and optical properties, such as richness, line-of-sight velocity dispersion of member galaxies, and shear due to gravitational lensing (e.g. Ortiz-Gil et al. 2004; Vikhlinin et al. 2006; Rozo et al. 2009; Sifón et al. 2013; Nastasi et al. 2014; von der Linden et al. 2014; Hoekstra et al. 2015). Scaling relations are power laws between galaxy cluster properties that have the potential to allow us to measure the mass of clusters using easily observable properties such as the X-ray luminosity, X-ray temperature and the velocity dispersion. These power laws can be predicted if we assume clusters are formed in the manner described by Kaiser (1986). In this model, known as the self-similar model, all galaxy clusters and groups are essentially identical objects which have been scaled up or down (Maughan et al. 2012). Strong self-similarity refers to when galaxy clusters have been scaled by mass and weak self-similarity refers to a scaling due to the changing density of the Universe with redshift (Bower 1997). This model makes some key assumptions, as described by Kravtsov & Borgani (2012) and Maughan et al. (2012). The first assumption is that we are in an Einstein-de-Sitter Universe, $\Omega_m = 1$, so the clusters form via a single gravitational collapse at the observed redshift. Secondly, gravitational energy as a result of the collapse is the only source of energy to the intracluster medium (ICM). By introducing these assumptions we greatly simplify the problem so that properties of the density field depend on only two control parameters, the slope of the power spectrum of the initial perturbations and its normalization. The strong self-similarity determines the slope and is not expected to evolve with redshift while the weak self-similarity is responsible for the evolution of the normalization since in this simplified model it is due only to a change in density with redshift (Bryan & Norman 1998). The most commonly studied scaling relation is the luminosity–temperature relation (L_X – T), however there is still no consensus on how it evolves with redshift and if self-similarity holds. Some studies have found that the evolution of the normalization of this relation is consistent with self-similarity (e.g. Vikhlinin et al. 2002; Lumb et al. 2004; Maughan et al. 2006), while other studies have found zero or negative evolution (e.g. Ettori et al. 2004; Branchesi et al. 2007; Clerc et al. 2012, 2014; Hilton et al. 2012). Maughan et al. (2012) also found that the evolution of the L_X – T relation was not self-similar, but concluded that this could plausibly be explained by selection effects. In this paper we focus on the lesser studied relationship between the velocity dispersion of member galaxies (σ_v) and the X-ray temperature (T_X) of the ICM. Since the velocity dispersion is a measure of the kinetic energy of the galaxies in the cluster, and temperature is related to the kinetic energy of the gas, both the gas and galaxies are tracers of the gravitational potential. One would expect a self-similar relationship of the form $\sigma_v \propto T^{0.5}$, if clusters were formed purely due to the action of gravity (Quintana & Melnick 1982; Kaiser 1986; Voit 2005). However, almost all previous studies of the relation have found a steeper power-law slope

than this (see Table 1). The relation is also not expected to evolve with redshift. To date this has been tested only by Wu, Fang & Xu (1998) and Nastasi et al. (2014). Even then, all but four clusters in the Wu et al. (1998) sample are at $z < 0.5$. Nastasi et al. (2014) made a measurement of the relation at $0.6 < z < 1.5$ using a sample of 12 clusters, obtaining results consistent with previous studies at low redshift. One may expect evolution in cluster scaling relations due to the increase of star formation and AGN activity at high redshift (e.g. Silverman et al. 2005; Magnelli et al. 2009), or due to the increase in frequency of galaxy cluster mergers with increasing redshift (e.g. Cohn & White 2005; Kay et al. 2007; Mann & Ebeling 2012). Galaxy cluster mergers are among the most energetic events in the Universe, and simulations have shown that these could result in the boosting of cluster X-ray temperatures (e.g. Randall, Sarazin & Ricker 2002; Ritchie & Thomas 2002; Poole et al. 2007). Fig. 9 in Ritchie & Thomas (2002) shows how the temperature is boosted when two equal mass systems have a head on collision with varying initial distances between their centres. All of these processes add energy into the ICM, and so we might expect to see an overall increase in the average temperatures of galaxy clusters above that expected from the self-similar case at a given redshift.

In this paper, we study a sample of 38 $z < 1.0$ galaxy clusters drawn from the *XMM* Cluster Survey (XCS; Mehrrens et al. 2012). We divide the sample into two groups: a low-redshift sample ($0.0 < z < 0.5$), and a high-redshift sample ($0.5 < z < 1.0$), such that each group has an equal number of clusters in each, and then proceed to test for evolution in the σ_v – T relation. We describe the sample and processing of the optical and X-ray data in Section 2. Section 3 discusses the method used to determine cluster membership and for measuring the velocity dispersion and describes the methods used for fitting the σ_v – T relation, and we present our results in Section 4. We discuss our findings in Section 5 and present our conclusions in Section 6. We assume a cosmology with $\Omega_m = 0.27$, $\Omega_\Lambda = 0.73$ and $H_0 = 70 \text{ km s}^{-1} \text{ Mpc}^{-1}$ throughout.

2 SAMPLE AND DATA REDUCTION

The cluster sample for this work is drawn from XCS, a serendipitous X-ray cluster survey being conducted using archival *XMM-Newton* data. Data Release 1 (DR1) of the XCS is described in Mehrrens et al. (2012). The overall aims of the XCS project are to measure cosmological parameters through the evolution of the cluster mass function with redshift (Sahlén et al. 2009), study the evolution of galaxies in clusters (Collins et al. 2009; Hilton et al. 2009, 2010; Stott et al. 2010) and investigate the X-ray scaling relations as a way to study the evolution of the cluster gas with redshift (Hilton et al. 2012). The XCS Automated Pipeline Algorithm (XAPA) described in Lloyd-Davies et al. (2011) was used to search the XMM archive for cluster candidates. Mehrrens et al. (2012) describes confirmation of a subset of these candidates as clusters using the combination of data from the literature and optical follow-up observations. This left a final sample of 503 X-ray confirmed galaxy clusters, 255 which were previously unknown and 356 of which were new X-ray detections. Of these, 464 have redshift estimates, and 402 have temperature measurements. For XCS-DR1 the cluster-averaged X-ray temperatures (T_X) were measured using an automated pipeline described in detail in Lloyd-Davies et al. (2011). In summary, this pipeline operates as follows: spectra were generated in the 0.3–7.9 keV band using photons in the XAPA source ellipse, (where the XAPA ellipse corresponds 0.08–0.56 of R_{500} , with a median value of to 0.36 R_{500} , where R_{500} is calculated using equation 2 and table 2 from Arnaud et al. 2005); an in-field background subtraction

Table 1. Previous measurements of the velocity dispersion–temperature relation. Here the relation is in the form $\sigma_v = 10^A T^B$, where σ_v is measured in km s^{-1} and T is measured in keV.

Paper	Number of clusters	A	B	Redshift range	Fitting method
Edge & Stewart (1991)	23	2.60 ± 0.08	0.46 ± 0.12	$z < 0.1$	Least squares
Lubin & Bahcall (1993)	41	2.52 ± 0.07	0.60 ± 0.11	$z < 0.2$	χ^2
Bird, Mushotzky & Metzler (1995)	22	2.50 ± 0.09	0.61 ± 0.13	$z < 0.1$	Bisector
Girardi et al. (1996)	37	2.53 ± 0.04	0.61 ± 0.05	$z < 0.2$	Bisector
Ponman et al. (1996)	27	2.54 ± 0.04	0.55 ± 0.05	$z < 0.15$	Bisector
White, Jones & Forman (1997)	35	2.53 ± 0.08	0.60 ± 0.10	$z < 0.2$	Orthogonal
Wu et al. (1998)	94	2.47 ± 0.06	0.67 ± 0.09	$z < 0.9$	Orthogonal
Wu et al. (1998)	110	2.57 ± 0.03	0.49 ± 0.05	$z < 0.1$	Orthogonal
Wu et al. (1998)	39	2.57 ± 0.08	0.56 ± 0.09	$0.1 < z < 0.9$	Orthogonal
Wu, Xue & Fang (1999)	92	2.49 ± 0.03	0.64 ± 0.02	$z < 0.45$	Orthogonal
Xue & Wu (2000)	109	2.53 ± 0.03	0.58 ± 0.05	$z < 0.2$	Orthogonal
Nastasi et al. (2014)	12	2.47 ± 0.19	0.64 ± 0.34	$0.64 < z < 1.46$	Bisector

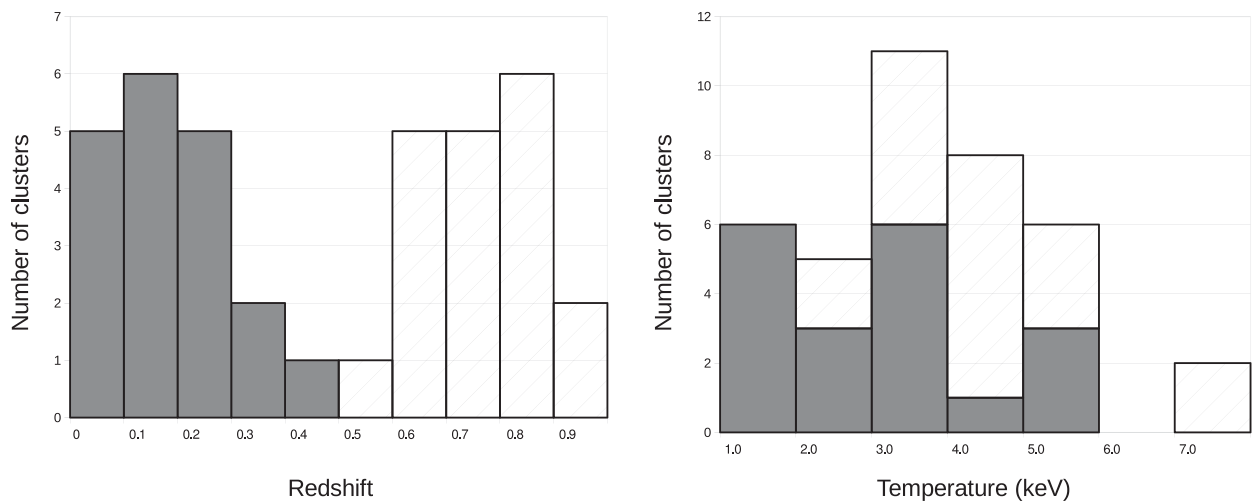


Figure 1. The redshift and temperature distributions of the low- and high-redshift cluster samples used in this work. The solid grey marks the low-redshift sample ($z < 0.5$) and the shading with diagonal lines marks the high-redshift sample ($z > 0.5$). Note that the high-redshift sample ($T_{\text{median}} = 4.5$ keV) contains more high-temperature clusters than the low-redshift sample ($T_{\text{median}} = 3.0$ keV).

method was used; and model fitting was done inside `XSPEC` (Schafer 1991) using an absorbed `MEKAL` (Mewe & Schrijver 1986) model and Cash statistics (Cash 1979). In the fit, the hydrogen column density was fixed to the Dickey (1990) value and the metal abundance to 0.3 times the solar value. For this paper, we have updated the T_x values compared to Mehtens et al. (2012). The pipeline is very similar to that described in Lloyd-Davies et al. (2011), but using updated versions of the `XMM` calibration and `XSPEC`. The median X-ray count for all the clusters in our final sample was 1919 with a minimum count of 220. We note that for only one of the clusters in our sample are the X-ray counts used for the spectral analysis less than 300. This is the minimum threshold defined by Lloyd-Davies et al. (2011) for reliable, i.e. with a fractional error of < 0.4 , T_x measurements at $T_x > 5$ keV (see fig. 16 from Lloyd-Davies et al. 2011). The remaining cluster was fit using 220 counts, but has a temperature of 3.5 keV (so still has an expected fractional error of 0.4) For this paper both the samples were constructed from XCS DR1, except for one of the high-redshift sample clusters (XMMXCS J113602.9–032943.2) which is a previously unreported XCS cluster detection. Fig. 1 shows the redshift and temperature distributions of the two samples. The high-redshift sample contains more high-temperature clusters than the low-redshift sample, which may be

due to selection effects which result in higher luminosity and hence higher temperature clusters being chosen at higher redshift.

2.1 Low-redshift sample

The low-redshift sample contains 19 clusters whose properties can be found in Table 3. In order to obtain this sample, we excluded all clusters from the DR1 sample that did not have temperatures or which had a redshift $z > 0.5$, leaving us with a sample of 320 clusters. We performed a search in NED¹ for galaxies surrounding each cluster. We included only clusters which had spectroscopic redshifts resulting in our sample size being decreased from 320 to 296. Since NED collects data from many different sources the reliability of the redshifts cannot be guaranteed. Hence, where possible we use only one source of redshifts per cluster to ensure homogeneity. These redshifts are specified to the fourth decimal place but

¹ This research has made use of the NASA/IPAC Extragalactic Database (NED) which is operated by the Jet Propulsion Laboratory, California Institute of Technology, under contract with the National Aeronautics and Space Administration.

unfortunately for most an uncertainty is not included in the original sample and therefore we assumed an accuracy of 1 per cent. We excluded galaxies located at a projected radial distance $>R_{200}$ (the radius within which the mean density is 200 times the critical density of the Universe at the cluster redshift) as such galaxies are unlikely to be cluster members. To ensure we did not exclude possible members, for this initial step R_{200} was calculated using a fiducial velocity dispersion of 2000 km s^{-1} following Finn et al. (2005),

$$R_{200} (\text{Mpc}) = 2.47 \frac{\sigma_v}{1000 \text{ km s}^{-1}} \frac{1}{\sqrt{\Omega_\Lambda + \Omega_0(1+z)^3}}. \quad (1)$$

Here, σ_v is the line-of-sight velocity dispersion (see Section 3.1.3) and z is the redshift of the cluster. Equation (1) assumes that the galaxy velocity distribution follows an isothermal sphere dark matter profile. The fiducial R_{200} values span the range 2–4 Mpc. Section 3.1.2 below describes how this initial cluster membership selection was refined to give the final cluster members. We then excluded all clusters which had less than 10 galaxies as this would provide us with two few members for accurate velocity dispersion calculation leaving us with a sample size of 19 clusters.

2.2 High-redshift sample

The high-redshift sample is made up of 19 clusters whose properties can be found in Table 4. Member redshifts were determined from observations using the Gemini telescopes for 12 of these clusters (see Section 2.2.1). The other seven clusters used data obtained from Nastasi et al. (2014). They drew both on new observations and on existing data. For example, the observations of three of the Nastasi et al. (2014) clusters we have used in this paper (XMMXCS J105659.5–033728.0, XMMXCS J113602.9–032943.2 and XMMXCS J182132.9+682755.0 in Table 4) were presented in Tran et al. (1999), respectively. The observations of the other four clusters we have used in this paper were presented for the first time in Nastasi et al. (2014). These four were discovered independently (to XCS) by the XMM Newton Distant Cluster Project (XDCP; Fassbender et al. 2011). Nastasi et al. (2014) also presented galaxy redshift data for another six XDCP clusters, however we have not used those in this paper because there are insufficient galaxies to derive an accurate velocity dispersion.² For the seven clusters that relied on Nastasi et al. (2014) data, new temperatures were obtained using XCS pipelines and the velocity dispersion was recalculated using the Nastasi et al. (2014) cluster redshift together with the method described in Section 3.

2.2.1 Observations

Observations of 12 $z > 0.5$ clusters were obtained using the Gemini Multi Object Spectrographs (GMOS) on both the Gemini telescopes from 2010 to 2012. The nod-and-shuffle mode (Glazebrook & Bland-Hawthorn 2001) was used to allow better sky subtraction and shorter slit lengths when compared to conventional techniques. For all observations the R400 grating and OG515 order blocking filter were used, giving wavelength coverage of 5400–9700 Å. The GMOS field-of-view samples out to R_{200} at the redshifts of our sample Sifón et al. (2013). A total of 30 masks were observed with a varying number of target slitlets. Each slitlet had length 3 arcsec and width 1 arcsec. Target galaxies were selected to be fainter

than the brightest cluster galaxy (which was also targeted in the slit masks), on the basis of *i*-band pre-imaging obtained from Gemini. We also used colour or photo- z information, where available, to maximize our efficiency in targeting cluster members. For five clusters which had *r*, *z*-band photometry from the National Optical Astronomy Observatory–XMM Cluster Survey (NXS; described in Mehrrens et al. 2012), we preferentially selected galaxies with *r* – *z* colours expected for passively evolving galaxies at the cluster redshift (see Mehrrens et al. 2012, for details). For four clusters, we used photometric redshifts for galaxies from SDSS DR7 (Abazajian et al. 2009). For XMMXCS J113602.9–032943.2, we used galaxy photo- z s that were measured from our own *riz* photometry obtained at the William Herschel Telescope on 2011 May 5. Observations at three different central wavelengths (7500, 7550 and 7600 Å) were used to obtain coverage over the gaps between the GMOS CCDs. For all observations an 85 percentile image quality and 50 percentile sky transparency were requested. The details of the individual observations are given in Table A1.

2.2.2 Spectroscopic data reduction

The data were reduced in a similar manner to Hilton et al. (2010), using PYRAF and the Gemini IRAF³ package. We used the tools from this package to subtract bias frames; make flat-fields; apply flat-field corrections and create mosaic images. We then applied nod-and-shuffle sky subtraction using the `gnsskysub` task. Wavelength calibration was determined from arc frames taken between the science frames, using standard IRAF tasks. All data were then combined using a median, rejecting bad pixels using a mask constructed from the nod-and-shuffle dark frames. Finally, we combined the pairs of spectra corresponding to each nod position, and extracted one-dimensional spectra using a simple boxcar algorithm.

2.2.3 Galaxy redshift measurements

We measured galaxy redshifts from the spectra by cross-correlation with SDSS spectral templates⁴ using the RVSAO/XCSAO package for IRAF (Kurtz & Mink 1998). XCSAO implements the method described by Tonry & Davis (1979). The spectra were compared to six different templates over varying redshifts with the final redshift measurement being determined after visual inspection. Redshifts were assigned a quality flag according to the following scheme: $Q = 3$ corresponds to two or more strongly detected features; $Q = 2$ refers to one strongly detected or two weakly detected features; $Q = 1$ one weakly detected feature and $Q = 0$ when no features could be identified. The features used were spectral lines, with the most commonly identified being [O II] 3727 Å, H, K, H β and the [O III] 4959, 5007 Å lines. Only galaxies with a quality rating of $Q \geq 2$ were used in this study because these have reasonably secure redshifts. Fig. 2 shows spectra of some member galaxies of the cluster XMMXCS J025006.4–310400.8 as an example. Tables of redshifts for galaxies in each cluster field as well as histograms depicting the included/excluded members and the best-fitting Gaussian can be found in Appendices B and C, respectively. Table 2 is shown, as an example, below for cluster XMMXCS J025006.4–310400.8.

² The methodology described in Section 3 was applied to these six clusters before they were excluded from our study.

³ IRAF is distributed by the National Optical Astronomy Observatories, which are operated by the Association of Universities for Research in Astronomy, Inc., under cooperative agreement with the National Science Foundation.

⁴ <http://www.sdss.org/dr7/algorithms/spectemplates/index.html>

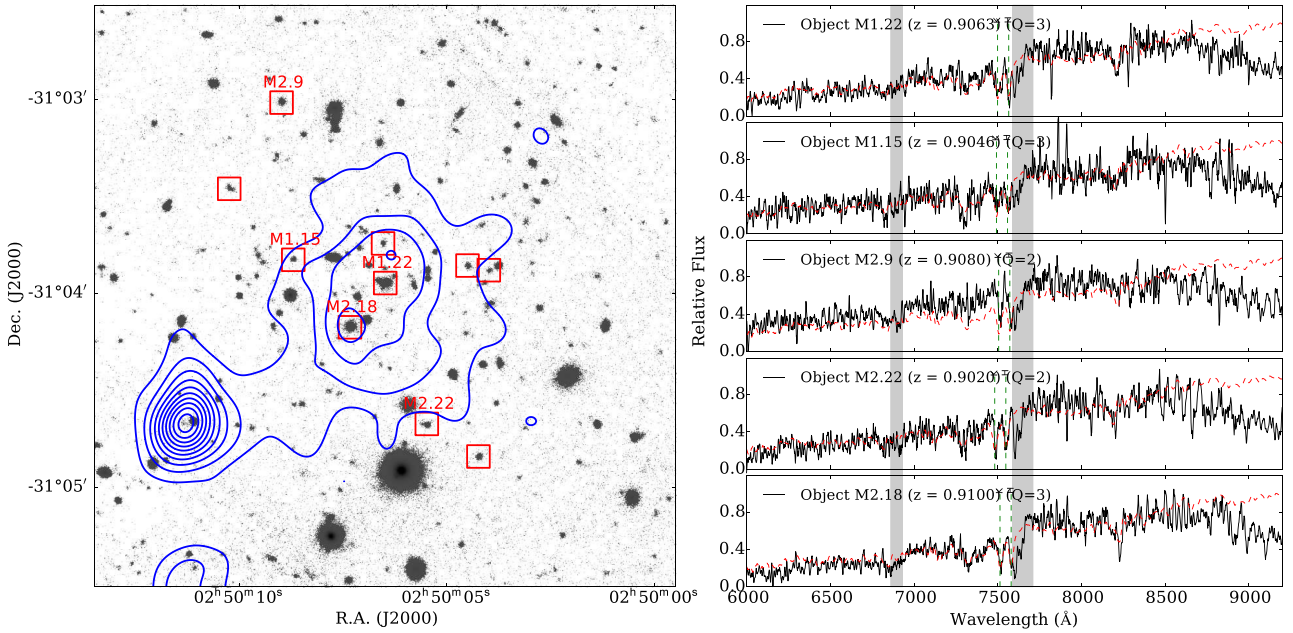


Figure 2. The $z = 0.91$ cluster XMMXCS J025006.4 – 310400.8. The left-hand panel shows the Gemini i -band image overlaid with the X-ray contours in blue. The red squares represent possible galaxy cluster members. Each possible member is labelled Mx.y, where x is the mask number and y is the object ID. The right-hand panel shows the Gemini spectra (black lines) for a subset of these galaxies. The grey bands indicate regions affected by telluric absorption lines. The red line is the best-fitting SDSS template. The green dotted vertical lines show the positions of the H and K lines at the galaxy redshift.

3 ANALYSIS

3.1 Membership determination and velocity dispersion measurements

In this section we describe the methodology used to determine cluster membership and calculate the velocity dispersion of each cluster.

3.1.1 Cluster redshifts

For all of the clusters an estimate of the redshift is known either from the literature or from previous observations and this is used as a starting point. The peculiar velocity of each of the galaxies is calculated relative to this redshift estimate using

$$v_i = c \times \frac{z_i - \bar{z}}{1 + \bar{z}}, \quad (2)$$

where v_i is the peculiar velocity of the i th galaxy, z_i is the redshift of the i th galaxy, \bar{z} is the redshift of the cluster and c is the speed of light. Extreme foreground and background sources were removed by applying a 3000 km s^{-1} cut with respect to the cluster redshift and then the redshift was recalculated using the biweight location method described by Beers, Flynn & Gebhardt (1990). This process was iterated until the redshift converged.

3.1.2 Cluster membership

A fixed gapper method, similar to that of Fadda et al. (1996) and Crawford, Wirth & Bershady (2014), was applied to determine which galaxies are cluster members. The reasoning behind this method is that by studying a histogram of the redshifts of possible members there should be a clear distinction between the cluster and the fore/background galaxies. Therefore we can exclude interlopers by finding the velocity difference between adjacent galaxies and

setting a fixed gap that should not be exceeded. De Propriis et al. (2002) found this optimum gap to be 1000 km s^{-1} , which avoids the merging of subclusters but also prevents the breaking up of real systems into smaller groups. Therefore all our galaxies were sorted by peculiar velocity and the difference between all adjacent pairs was calculated. Any galaxies which had a difference between adjacent galaxies of greater than 1000 km s^{-1} were considered interlopers and were removed. This process was iterated until the number of galaxies converged.

3.1.3 Velocity dispersion

We used our confirmed galaxy cluster members to calculate an initial estimate of the velocity dispersion of each cluster using the biweight scale method described in Beers et al. (1990). We then calculated R_{200} using equation (1), and excluded all galaxies located at projected cluster-centric radial distances outside R_{200} . The velocity dispersion of each cluster was then recalculated. This final radial cut did not remove more than two galaxies from the final sample for each cluster. Tables 3 and 4 list the final redshifts, velocity dispersions and R_{200} values for the low- and high-redshift samples, respectively.

3.2 Fitting the velocity dispersion–temperature relation

To determine the scaling relation between the velocity dispersion and temperature, we fitted a power law of the form

$$\log \left(\frac{\sigma_v}{1000 \text{ km s}^{-1}} \right) = A + B \log \left(\frac{T}{5 \text{ keV}} \right) + C \log E(z). \quad (3)$$

Here, 5 keV and 1000 km s^{-1} are the pivot temperature and velocity dispersion, respectively, for our fit. These were chosen to reduce the covariance between the normalization A and the slope B , and for ease of comparison to previous studies. In the above,

Table 2. We depict the galaxy redshifts for the cluster XMMXCS J025006.4–310400.8. Column 1 gives an arbitrary ID for each galaxy, columns 2 and 3 give the right ascension and declination, respectively, and column 4 gives the redshift of the galaxy. Column 5 gives the quality flag as explained in Section 2.2.3 and column 6 shows whether or not the galaxy was included as a member for the determination of the velocity dispersion.

ID	Mask	RA(J2000)	Dec(J2000)	z	Quality	Member
1	GS-2010B-Q-46-06	02 ^h 50 ^m 22 ^s .92	−31°03′53″.0	0.8337	3	
8	GS-2010B-Q-46-06	02 ^h 50 ^m 15 ^s .25	−31°03′33″.5	0.7263	3	
9	GS-2010B-Q-46-06	02 ^h 50 ^m 13 ^s .27	−31°03′35″.7	0.6168	3	
10	GS-2010B-Q-46-06	02 ^h 50 ^m 12 ^s .05	−31°03′08″.0	0.7146	3	
14	GS-2010B-Q-46-06	02 ^h 50 ^m 06 ^s .63	−31°03′13″.7	0.8496	3	
15	GS-2010B-Q-46-06	02 ^h 50 ^m 08 ^s .70	−31°03′49″.7	0.9052	3	✓
16	GS-2010B-Q-46-06	02 ^h 50 ^m 03 ^s .78	−31°03′51″.5	0.3533	3	
17	GS-2010B-Q-46-06	02 ^h 50 ^m 06 ^s .89	−31°03′51″.5	0.9217	3	✓
18	GS-2010B-Q-46-06	02 ^h 50 ^m 05 ^s .48	−31°03′53″.0	0.6972	3	
19	GS-2010B-Q-46-06	02 ^h 50 ^m 04 ^s .50	−31°03′51″.5	0.9149	3	✓
21	GS-2010B-Q-46-06	02 ^h 50 ^m 02 ^s .79	−31°04′04″.9	0.9831	3	
22	GS-2010B-Q-46-06	02 ^h 50 ^m 06 ^s .48	−31°03′56″.9	0.9069	3	✓
23	GS-2010B-Q-46-06	02 ^h 50 ^m 09 ^s .04	−31°04′06″.3	0.7567	3	
25	GS-2010B-Q-46-06	02 ^h 50 ^m 03 ^s .83	−31°04′34″.0	0.8988	3	✓
26	GS-2010B-Q-46-06	02 ^h 50 ^m 04 ^s .24	−31°04′50″.6	0.9095	3	✓
28	GS-2010B-Q-46-06	02 ^h 50 ^m 04 ^s .59	−31°05′41″.7	0.6197	3	
34	GS-2010B-Q-46-06	02 ^h 50 ^m 04 ^s .26	−31°07′05″.2	0.1261	3	
1	GS-2012B-Q-011-09	02 ^h 50 ^m 22 ^s .92	−31°03′53″.0	0.5924	2	
2	GS-2012B-Q-011-09	02 ^h 50 ^m 18 ^s .11	−31°03′10″.5	0.9326	2	
4	GS-2012B-Q-011-09	02 ^h 50 ^m 16 ^s .05	−31°03′23″.1	1.0077	2	
5	GS-2012B-Q-011-09	02 ^h 50 ^m 14 ^s .89	−31°03′32″.1	0.7245	3	
6	GS-2012B-Q-011-09	02 ^h 50 ^m 14 ^s .94	−31°02′56″.8	0.9927	2	
9	GS-2012B-Q-011-09	02 ^h 50 ^m 08 ^s .98	−31°03′01″.1	0.9086	3	✓
10	GS-2012B-Q-011-09	02 ^h 50 ^m 10 ^s .24	−31°03′27″.8	0.9056	3	✓
11	GS-2012B-Q-011-09	02 ^h 50 ^m 07 ^s .01	−31°01′00″.9	0.5204	3	
13	GS-2012B-Q-011-09	02 ^h 50 ^m 06 ^s .54	−31°03′44″.7	0.9126	3	✓
17	GS-2012B-Q-011-09	02 ^h 50 ^m 03 ^s .99	−31°03′53″.0	0.9176	3	✓
18	GS-2012B-Q-011-09	02 ^h 50 ^m 07 ^s .33	−31°04′10″.6	0.9106	3	✓
19	GS-2012B-Q-011-09	02 ^h 50 ^m 02 ^s .67	−31°03′26″.0	0.9797	3	
20	GS-2012B-Q-011-09	02 ^h 50 ^m 07 ^s .38	−31°05′28″.7	0.6494	2	
21	GS-2012B-Q-011-09	02 ^h 49 ^m 58 ^s .10	−31°03′39″.6	0.8696	3	✓
22	GS-2012B-Q-011-09	02 ^h 50 ^m 05 ^s .48	−31°04′40″.5	0.9026	2	
27	GS-2012B-Q-011-09	02 ^h 49 ^m 58 ^s .68	−31°05′25″.8	0.6274	3	
28	GS-2012B-Q-011-09	02 ^h 49 ^m 59 ^s .99	−31°05′07″.8	0.8816	2	
29	GS-2012B-Q-011-09	02 ^h 49 ^m 58 ^s .60	−31°04′59″.2	0.9216	3	✓
30	GS-2012B-Q-011-09	02 ^h 50 ^m 00 ^s .51	−31°04′44″.5	0.5654	3	
31	GS-2012B-Q-011-09	02 ^h 50 ^m 04 ^s .26	−31°07′05″.2	0.9827	3	

evolution of the normalization is parametrized as $E(z)^C$, where $E(z) = \sqrt{\Omega_m(1+z)^3 + \Omega_\Lambda}$ describes the redshift evolution of the Hubble parameter. For the self-similar case, $B = 0.5$ and $C = 0$ are expected. Similarly to Hilton et al. (2012), the best-fitting values for these parameters were found using Markov Chain Monte Carlo (MCMC) with the Metropolis algorithm. Both orthogonal and bisector regression methods were used. For the orthogonal method, the probability for a given cluster to be drawn from the model scaling relation is

$$P_{\text{model}} = \frac{1}{\sqrt{2\pi(\Delta r^2 + \Delta S^2)}} \exp\left[-\frac{(r - r_{\text{model}})^2}{2(\Delta r^2 + S^2)}\right], \quad (4)$$

where $r - r_{\text{model}}$ is the orthogonal distance of the cluster from the model relation, Δr is the error on the orthogonal distance and S is the intrinsic scatter orthogonal to the model relation. Δr is calculated from the projection in the direction orthogonal to the model line of the ellipse defined by the errors on $\log \sigma_v$ and $\log T$, chosen according to the position of a given point relative to the model fit line. For the bisector method, the intrinsic scatter and measurement errors are treated independently for each axis. Therefore in the

equation for P_{model} , r_{model} is replaced by

$$y_{\text{model}} = \log\left(\frac{\sigma_v}{1000 \text{ km s}^{-1}}\right) - \left[A + B \log\left(\frac{T}{5 \text{ keV}}\right) + C \log E(z)\right], \quad (5)$$

and

$$x_{\text{model}} = \log\left(\frac{T}{5 \text{ keV}}\right) - \left[\frac{\log\left(\frac{\sigma_v}{1000 \text{ km s}^{-1}}\right) - A - C \log E(z)}{B}\right], \quad (6)$$

where r and Δr are replaced by x , Δx or y , Δy as appropriate. The intrinsic scatter S is replaced by two parameters S_x and S_y . For both methods, the likelihood \mathcal{L} of a given model is simply the product of P_{model} for each cluster in the sample, i.e. in the orthogonal case

$$\mathcal{L}(\sigma_v, T|A, B, C, S) \propto P_{\text{prior}}(A, B, C, S) \prod_i P_{\text{model},i}, \quad (7)$$

where we assume generous, uniform priors on each parameter, as listed in Table 5.

Table 3. Low-redshift sample ($0.0 < z < 0.5$): column 1 gives the name of the XCS cluster, columns 2 and 3 give its J2000 right ascension and declination. Column 4 gives the redshift, with the uncertainty found using bootstrapping and column 5 gives the redshift from literature. Column 6 gives the temperature with its positive and negative 1σ uncertainty. Column 7 gives the number of confirmed members and columns 8 and 9 give the calculated velocity dispersion and R_{200} , respectively. The references for the redshifts are as follows: 1. Mehrrens et al. (2012), 2. Cappi, Held & Marano (1998), 3. Yoon et al. (2008), 4. Mulchaey et al. (2006), 5. Vikhlinin et al. (1998), 6. Takey, Schwoppe & Lamer (2013), 7. Finoguenov et al. (2007), 8. Takey, Schwoppe & Lamer (2011), 9. Hao et al. (2010), 10. Hennawi et al. (2008), 11. Struble & Rood (1999), 12. Burenin et al. (2007), 13. Koester et al. (2007), 14. Mullis et al. (2003) and 15. Sakelliou & Merrifield (1998).

Name	RA (J2000)	Dec (J2000)	z	z_{lit}	T (keV)	Members	σ_v (km s $^{-1}$)	R_{200} (Mpc)
XMMXCS J000013.9–251052.1	00 ^h 00 ^m 13 ^s .9	–25°10′52″.1	0.0845 ± 0.0004	0.08 ¹	1.80 ^{+0.40} _{–0.20}	19	410 ± 80	1.11
XMMXCS J003430.1–431905.6	00 ^h 34 ^m 30 ^s .1	–43°19′05″.6	0.3958 ± 0.0010	0.40 ¹	3.50 ^{+0.20} _{–0.20}	22	920 ± 150	1.96
XMMXCS J005603.0–373248.0	00 ^h 56 ^m 03 ^s .0	–37°32′48″.0	0.1659 ± 0.0009	0.16 ²	5.20 ^{+0.30} _{–0.20}	22	900 ± 140	2.06
XMMXCS J015315.0+010214.2	01 ^h 53 ^m 15 ^s .0	+01°02′14″.2	0.0593 ± 0.0002	0.06 ³	1.08 ^{+0.02} _{–0.02}	12	240 ± 80	0.55
XMMXCS J072054.3+710900.5	07 ^h 20 ^m 54 ^s .3	+71°09′00″.5	0.2309 ± 0.0005	0.23 ⁴	2.90 ^{+0.50} _{–0.40}	29	550 ± 60	1.20
XMMXCS J081918.6+705457.5	08 ^h 19 ^m 18 ^s .6	+70°54′57″.5	0.2298 ± 0.0005	0.23 ⁵	3.00 ^{+0.80} _{–0.60}	19	410 ± 70	0.83
XMMXCS J094358.2+164120.7	09 ^h 43 ^m 58 ^s .2	+16°41′20″.7	0.2539 ± 0.0005	0.25 ¹	1.50 ^{+0.40} _{–0.20}	27	590 ± 90	1.54
XMMXCS J095957.6+251629.0	09 ^h 59 ^m 57 ^s .6	+25°16′29″.0	0.0523 ± 0.0005	0.08 ⁶	1.40 ^{+0.05} _{–0.05}	15	510 ± 220	1.79
XMMXCS J100047.4+013926.9	10 ^h 00 ^m 47 ^s .4	+01°39′26″.9	0.2202 ± 0.0006	0.22 ⁷	3.30 ^{+0.20} _{–0.20}	16	560 ± 140	1.41
XMMXCS J100141.7+022539.8	10 ^h 01 ^m 41 ^s .7	+02°25′39″.8	0.1233 ± 0.0005	0.12 ⁸	1.43 ^{+0.06} _{–0.03}	26	590 ± 130	1.05
XMMXCS J104044.4+395710.4	10 ^h 40 ^m 44 ^s .4	+39°57′10″.4	0.1389 ± 0.0007	0.16 ⁹	3.54 ^{+0.03} _{–0.03}	17	860 ± 150	2.12
XMMXCS J111515.6+531949.5	11 ^h 15 ^m 15 ^s .6	+53°19′49″.5	0.4663 ± 0.0010	0.47 ¹⁰	5.40 ^{+1.50} _{–0.90}	16	910 ± 310	1.75
XMMXCS J115112.0+550655.5	11 ^h 51 ^m 12 ^s .0	+55°06′55″.5	0.0791 ± 0.0003	0.08 ¹¹	1.66 ^{+0.04} _{–0.04}	16	330 ± 100	1.50
XMMXCS J123144.4+413732.0	12 ^h 31 ^m 44 ^s .4	+41°37′32″.0	0.1735 ± 0.0009	0.18 ¹²	2.70 ^{+0.60} _{–0.40}	10	480 ± 100	1.26
XMMXCS J151618.6+000531.3	15 ^h 16 ^m 18 ^s .6	+00°05′31″.3	0.1200 ± 0.0005	0.13 ¹³	5.40 ^{+0.10} _{–0.10}	35	870 ± 220	2.01
XMMXCS J161132.7+541628.3	16 ^h 11 ^m 32 ^s .7	+54°16′28″.3	0.3372 ± 0.0013	0.33 ⁸	4.60 ^{+1.20} _{–0.80}	12	790 ± 150	1.69
XMMXCS J163015.6+243423.2	16 ^h 30 ^m 15 ^s .6	+24°34′23″.2	0.0625 ± 0.0003	0.07 ¹⁴	3.50 ^{+0.60} _{–0.40}	62	710 ± 130	2.20
XMMXCS J223939.3–054327.4	22 ^h 39 ^m 39 ^s .3	–05°43′27″.4	0.2451 ± 0.0003	0.24 ¹⁴	2.80 ^{+0.20} _{–0.20}	68	560 ± 70	1.32
XMMXCS J233757.0+271121.0	23 ^h 37 ^m 57 ^s .0	+27°11′21″.0	0.1237 ± 0.0007	0.12 ¹⁵	3.40 ^{+0.60} _{–0.40}	12	460 ± 110	1.49

4 RESULTS

4.1 Evolution of the slope and intrinsic scatter

For the model given in equation (3), it is assumed that the slope (parameter B) is not evolving with redshift. To test this, the σ_v-T relation was fitted with $C = 0$ in two redshift bins, $0.0 < z < 0.5$ and $0.5 < z < 0.9$, with 19 clusters in each bin. The parameters A , B and S were obtained using the MCMC method described above for the high- and low-redshift samples individually. The results for this are shown in Figs 3 and 4. Using the orthogonal method we found $B = 1.12 \pm 0.41$ for the high-redshift sample and $B = 0.89 \pm 0.16$ for the low-redshift sample. However, we found that the slope of the relation for the high-redshift sample is unconstrained if the prior on B is relaxed further. We assume for the remainder of this paper that the slope does not evolve with redshift, though clearly either a larger sample or more accurate measurements of individual clusters are needed to confirm that this is true. The intrinsic scatter is $S = 0.05 \pm 0.02$ for the low-redshift sample and $S = 0.08 \pm 0.04$ for the high-redshift sample. Therefore there is no evidence that the intrinsic scatter varies with redshift.

4.2 Evolution of the normalization

To test for the evolution of the normalization (parameter A in equation 3), the low- and high-redshift samples were combined and C was allowed to vary in the MCMC analysis. The results obtained are shown in Figs 6 and 7. We found $C = -0.53 \pm 0.27$, meaning that for a given σ_v , a higher T is obtained at higher redshift.

However, the no evolution relation falls within the 95 per cent confidence interval and therefore we conclude that there is no significant evidence in favour of evolution.

We also applied a statistical test known as the Akaike information criterion (AIC) to determine whether the model with or without evolution (Fig. 5) was preferred. The AIC estimates the quality of each model relative to each other and is therefore a means of model selection. It is defined by (Burnham & Anderson 2002) as

$$\text{AIC} = 2k - 2\ln(\mathcal{L}), \quad (8)$$

where \mathcal{L} is the maximized likelihood function (equation 7) and k is the number of free parameters. The AIC includes a penalty for using extra parameters as a way to discourage overfitting and rewards goodness of fit based on the likelihood function. Therefore the lower the value of the AIC, the better the fit. For the combined sample with the no evolution model the AIC value was -64.6 and when the fourth parameter for evolution (C) was included this increased to -62.1 . Therefore, combining this with the results from the σ_v-T relation fit, it can be concluded that the preferred model is the one with no evolution of the normalization of the scaling relation.

5 DISCUSSION

5.1 Comparison with previous results

Table 6 and Figs 3–6 present the results of applying the orthogonal and bisector fitting methods to the low redshift, high redshift and combined samples. We see that the bisector and orthogonal method

Table 4. High-redshift sample ($0.5 < z < 1.0$): all columns are as explained in Table 3. The superscripts in column one indicate the origin of redshift data when it did not come from our own observations; ^aare all clusters taken from the XDCP survey and were observed with the VLT-FORS2 spectrograph (Nastasi et al. 2014), ^balso known as MS1054-03 was observed with Keck for 8.6 h (Tran et al. 1999), ^cwas observed with Keck (Donahue et al. 1999), ^dalso known as RXJ1821.6+6827 was observed with CFHT, Keck and the 2.2 m telescope at the University of Hawaii (Gioia et al. 2004). The references for the redshifts are as follows: 1. Nastasi et al. (2014), 2. Scharf et al. (1997), 3. Mehtens et al. (2012), 4. Adami et al. (2011), 5. Šuhada et al. (2011), 6. Bellagamba et al. (2011), 7. Gioia & Luppino (1994), 8. Basilakos et al. (2004), 9. Gioia et al. (2004) and 10. Perlman et al. (2002).

Name	RA (J2000)	Dec (J2000)	z	z_{lit}	T (keV)	Members	σ_v (km s ⁻¹)	R_{200} (Mpc)
^a XMMXCS J000216.1–355633.8	00 ^h 02 ^m 16 ^s .1	–35°56′33″.8	0.7709 ± 0.0021	0.77 ¹	4.83 ^{+1.015} _{–0.76}	13	1100 ± 190	1.77
XMMXCS J005656.6–274031.9	00 ^h 56 ^m 56 ^s .6	–27°40′31″.9	0.5601 ± 0.0007	0.56 ²	3.30 ^{+0.94} _{–0.63}	15	380 ± 60	0.66
XMMXCS J015241.1–133855.9	01 ^h 52 ^m 41 ^s .1	–13°38′55″.9	0.8268 ± 0.0010	0.82 ³	3.23 ^{+0.38} _{–0.31}	29	840 ± 150	1.33
XMMXCS J021734.7–051326.9	02 ^h 17 ^m 34 ^s .7	–05°13′26″.9	0.6467 ± 0.0012	0.65 ⁴	2.23 ^{+0.90} _{–0.44}	12	620 ± 210	1.11
XMMXCS J025006.4–310400.8	02 ^h 50 ^m 06 ^s .4	–31°04′00″.8	0.9100 ± 0.0024	0.90 ²	4.50 ^{+1.33} _{–0.88}	13	1120 ± 260	1.66
XMMXCS J030205.1–000003.6	03 ^h 02 ^m 05 ^s .1	–00°00′03″.6	0.6450 ± 0.0007	0.65 ⁵	5.82 ^{+2.09} _{–1.32}	16	610 ± 180	1.04
^a XMMXCS J095417.1+173805.9	09 ^h 54 ^m 17 ^s .1	17°38′05″.9	0.8272 ± 0.0017	0.82 ¹	3.65 ^{+0.62} _{–0.51}	10	940 ± 310	1.42
XMMXCS J095940.7+023113.4	09 ^h 59 ^m 40 ^s .7	+02°31′13″.4	0.7291 ± 0.0005	0.72 ⁶	5.02 ^{+0.68} _{–0.55}	25	470 ± 90	0.88
^b XMMXCS J105659.5–033728.0	10 ^h 56 ^m 59 ^s .5	–03°37′28″.0	0.8336 ± 0.0013	0.82 ⁷	7.57 ^{+0.43} _{–0.40}	29	1010 ± 120	1.57
XMMXCS J112349.4+052955.1	11 ^h 23 ^m 49 ^s .4	+05°29′55″.1	0.6550 ± 0.0007	0.65 ³	4.62 ^{+1.55} _{–0.95}	17	600 ± 210	1.05
XMMXCS J113602.9–032943.2	11 ^h 36 ^m 02 ^s .9	–03°29′43″.2	0.8297 ± 0.0011		3.32 ^{+1.20} _{–0.78}	21	700 ± 110	1.06
^c XMMXCS J114023.0+660819.0	11 ^h 40 ^m 23 ^s .0	+66°08′19″.0	0.7855 ± 0.0015	0.78 ⁷	7.47 ^{+0.92} _{–0.77}	22	950 ± 100	1.51
^a XMMXCS J124312.2–131307.2	12 ^h 43 ^m 12 ^s .2	–13°13′07″.2	0.7910 ± 0.0014	0.80 ¹	4.92 ^{+2.93} _{–1.54}	11	790 ± 460	1.19
XMMXCS J134305.1–000056.8	13 ^h 43 ^m 05 ^s .1	–00°00′56″.8	0.6894 ± 0.0011	0.67 ⁸	4.49 ^{+0.72} _{–0.57}	23	920 ± 170	1.72
XMMXCS J145009.3+090428.8	14 ^h 50 ^m 09 ^s .3	+09°04′28″.8	0.6412 ± 0.0007	0.60 ³	3.84 ^{+0.66} _{–0.55}	22	630 ± 90	1.07
^d XMMXCS J182132.9+682755.0	18 ^h 21 ^m 32 ^s .9	+68°27′55″.0	0.8166 ± 0.0011	0.82 ⁹	4.49 ^{+0.79} _{–0.56}	19	860 ± 130	1.34
XMMXCS J215221.0–273022.6	21 ^h 52 ^m 21 ^s .0	–27°30′22″.6	0.8276 ± 0.0011	0.82 ³	2.18 ^{+0.67} _{–0.45}	15	530 ± 150	0.86
XMMXCS J230247.7+084355.9	23 ^h 02 ^m 47 ^s .7	+08°43′55″.9	0.7187 ± 0.0014	0.72 ¹⁰	5.29 ^{+0.59} _{–0.50}	22	1010 ± 130	1.60
^a XMMXCS J235616.4–344144.3	23 ^h 56 ^m 16 ^s .4	–34°41′44″.3	0.9391 ± 0.0012	0.94 ¹	4.57 ^{+0.48} _{–0.41}	10	670 ± 260	0.91

Table 5. Priors on $\sigma_v - T$ relation fit parameters.

Parameter	Uniform prior	Notes
A	(–5.0,5.0)	–
B	(0.0,2.0)	–
C	(–1.0,1.0)	–
S	(0.01,1.0)	Orthogonal method only
S_x	(0.01,1.0)	Bisector method only
S_y	(0.01,1.0)	Bisector method only

give very similar results especially for our total sample without evolution. Hogg, Bovy & Lang (2010) suggest that the bisector method should be avoided, as by simply finding the difference between a forward and reverse fitting method large systematic errors will be introduced, but it has been widely used for scaling relation measurements in the past and is therefore included for completeness. Results from previous studies of the $\sigma_v - T$ relation are collected in Table 1. All of these studies, except for Edge & Stewart (1991) and the low-redshift sample of Wu et al. (1998), obtained a slope steeper than the expected self-similar slope of $\sigma_v \propto T^{0.5}$. We measured $B = 0.72 \pm 0.12$ using the orthogonal fitting method and $B = 0.77 \pm 0.08$ using the bisector fitting method for our combined sample. Therefore both the orthogonal and bisector slopes are in agreement with each other and the previous values in the literature, except for the result obtained by Edge & Stewart (1991) which is only consistent with the orthogonal result. Except for work done by Wu et al. (1998) and Nastasi et al. (2014), all the previous results were obtained for low-redshift samples and no test for evolution was performed. Wu et al. (1998) divided their sample into two

groups, $z < 0.1$ and $z \geq 0.1$, and found no significant evolution, however their sample included only four clusters in the redshift range $0.5 < z < 1.0$. Nastasi et al. (2014) had a sample of 12 galaxy clusters and found a very large error of more than 50 per cent on their slope. They concluded that their sample size was too small to accurately measure evolution. We conclude that the data presented in this paper – a homogeneous cluster sample that is larger than those used in previous studies at $z > 0.5$ – are consistent with previous results.

5.2 Description of simulations

Comparison to simulations are important for two main reasons. First, we can determine if there is any bias due to sample selection as the simulations provide both a bigger temperature and redshift range. It also allows us to compare different simulation models and learn about the nature of the non-gravitational physics through their effect on the gas temperature. The Millennium Gas Project is a set of hydrodynamical simulations described in Short et al. (2010) which uses the same initial perturbations as the Millennium Simulation (Springel et al. 2005). These simulations include a variety of models, including gravity only; energy injection with radiative cooling; and feedback only. For comparison to the data presented in this paper, the feedback only model (FO) in a volume of $250 h^{-1} \text{Mpc}^3$ was used. This model includes supernova and AGN feedback using a semi-analytic galaxy formation model. Heating due to supernovae and AGN and the star formation rate are obtained using the model of De Lucia & Blaizot (2007). The AGN feedback model used is described in Bower, McCarthy & Benson (2008), which is dependent on the matter accreted by the central black hole and the efficiency

Table 6. Best-fitting σ_v-T scaling relation parameters using both the orthogonal and bisector regression methods (see Section 3.2).

Method	Parameter	Low redshift	High redshift	Combined (no evolution)	Combined (with evolution)
Orthogonal	A	0.02 ± 0.06	-0.08 ± 0.05	-0.05 ± 0.04	0.02 ± 0.05
	B	0.89 ± 0.16	1.12 ± 0.41	0.72 ± 0.12	0.86 ± 0.14
	S	0.05 ± 0.03	0.08 ± 0.04	0.06 ± 0.03	0.06 ± 0.03
	C	0	0	0	-0.37 ± 0.33
Bisector	A	0.02 ± 0.04	-0.07 ± 0.03	-0.04 ± 0.02	0.02 ± 0.04
	B	0.85 ± 0.11	1.01 ± 0.17	0.77 ± 0.08	0.86 ± 0.09
	S_x	0.15 ± 0.03	0.19 ± 0.03	0.15 ± 0.02	0.14 ± 0.02
	S_y	0.07 ± 0.03	0.12 ± 0.04	0.09 ± 0.02	0.09 ± 0.02
	C	0	0	0	-0.49 ± 0.25

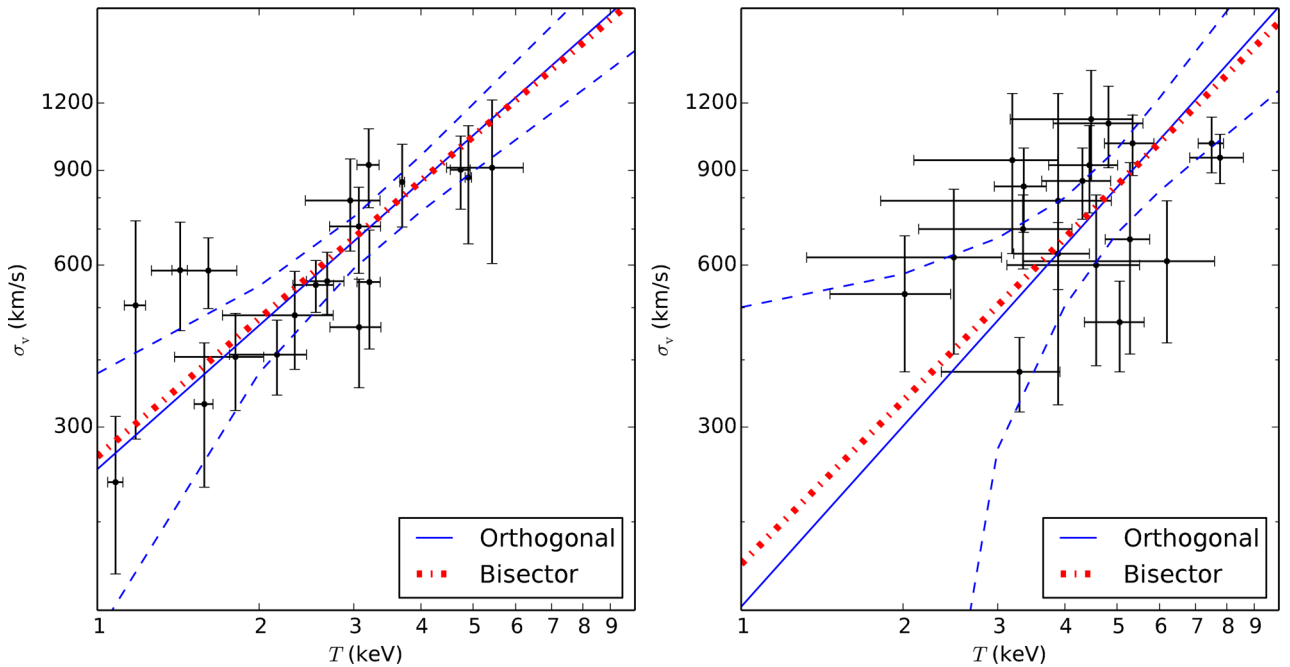


Figure 3. The σ_v-T relation assuming no evolution, i.e. $C = 0$ in equation (3), for low (left $-0.0 < z < 0.5$) and high (right $-0.5 < z < 0.9$) redshift samples. The solid blue line shows an orthogonal regression fit to the data with the dashed line representing the 95 per cent confidence interval. The dot-dashed line shows a bisector regression fit to the data (see Section 3.2). A model of the form seen in equation (3) was used in the Metropolis algorithm to determine a line of best fit (see Section 4.1). It is interesting to note that the two best-measured systems (XMMXCS J105659.5–033728.0 and XMMXCS J114023.0+660819.0) in the high-redshift subsample are relatively far off the best-fitting relation, with a higher than predicted temperature. Our current observations do not provide good enough spatial resolution or deep enough multicolour photometry to determine the exact reason for this and require further study and re-observations.

with which the matter is converted to energy near the event horizon, with the upper limit being at 2 per cent of the Eddington rate. As a comparison to the velocity dispersion of the cluster, two proxies were considered, the velocity dispersion of the stars (σ_{Stars}) and that obtained from the dark matter particles (σ_{DM}). The temperatures used from the simulation were spectroscopic-like temperatures (T_{Sl} ; Mazzotta et al. 2004). To ensure that only clusters similar to those in our sample were included, we excluded all groups from the simulation with a mass less than $10^{14} M_{\odot}$. We also included a temperature cut, $2 < T(\text{keV}) < 11$, and a redshift cut, $0 < z < 1$, to match our sample. We also compared to the results of the BAHAMAS hydrodynamical simulation (McCarthy et al. 2016 and Caldwell et al. in preparation). Here, a $400 h^{-1} \text{Mpc}^3$ box is used, with initial conditions based on Planck 2013 cosmological parameters (Planck Collaboration XVI 2014), and both AGN and supernovae feedback models as described by Le Brun et al. (2014). A galaxy mass lower limit of $5 \times 10^9 M_{\odot}$ and a cluster mass lower limit of $10^{14} M_{\odot}$ were

implemented. This simulation reproduces a large number of X-ray, SZ and optical scaling relations of groups and clusters. However, unlike previous simulations, the new simulation also reproduces the observed galaxy stellar mass function remarkably well over a wide range of stellar masses. The velocity dispersion is traced by galaxies and is calculated using the gapper technique described by Beers et al. (1990). The temperatures used from the simulation were spectroscopic (T_{S}). We note that spectroscopic-like temperatures, as used in both simulations, are most robust at $T > 2 \text{keV}$, where the bremsstrahlung mechanism dominates (Short et al. 2010). Therefore, while we have applied mass, temperature and redshift cuts to the simulated cluster catalogues that are a reasonable match to our observed sample, the correspondence is not exact, as six of the observed clusters have $T < 2 \text{keV}$. This is a compromise aimed at limiting the potential impact of low-mass clusters with less reliable temperature measurements in the simulations. Matching the velocity dispersions to the simulations, however, is not as

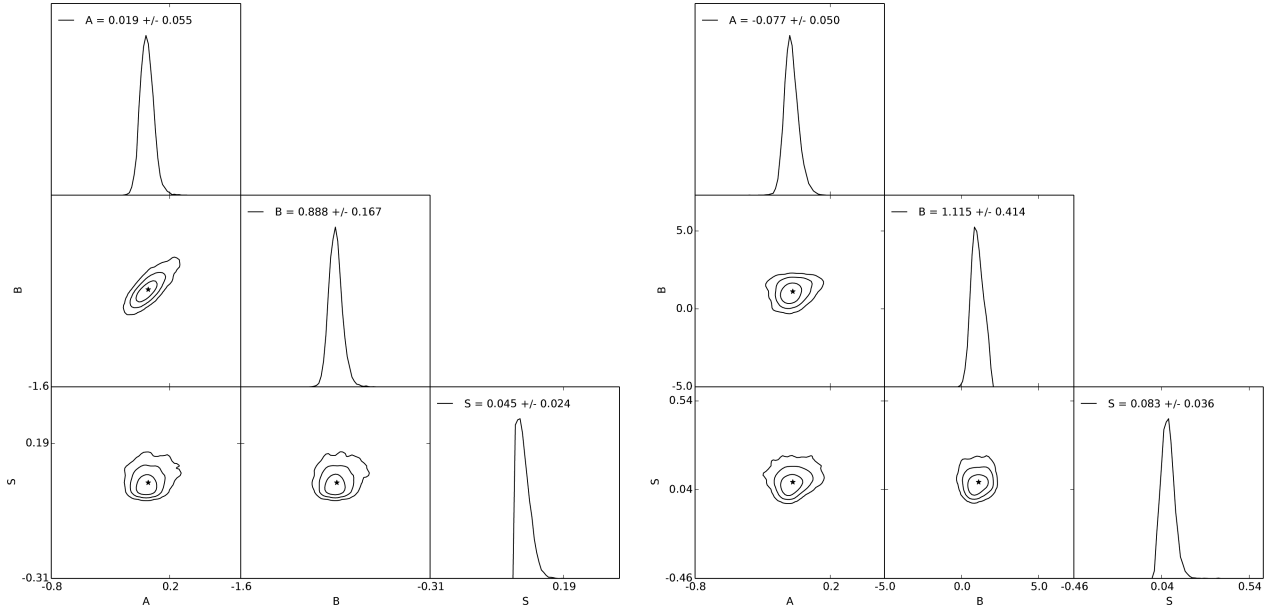


Figure 4. Corner plots for the low (left $-0.0 < z < 0.5$) and high (right $-0.5 < z < 0.9$) redshift sample showing all the one and two-dimensional projections of the posterior probability distributions of the three parameters when using the orthogonal method. The values of each parameter are given in the top centre. The histograms show the one-dimensional marginalized distribution for each parameter and the other plots show the two-dimensional version, where the contours show 1σ , 2σ and 3σ .

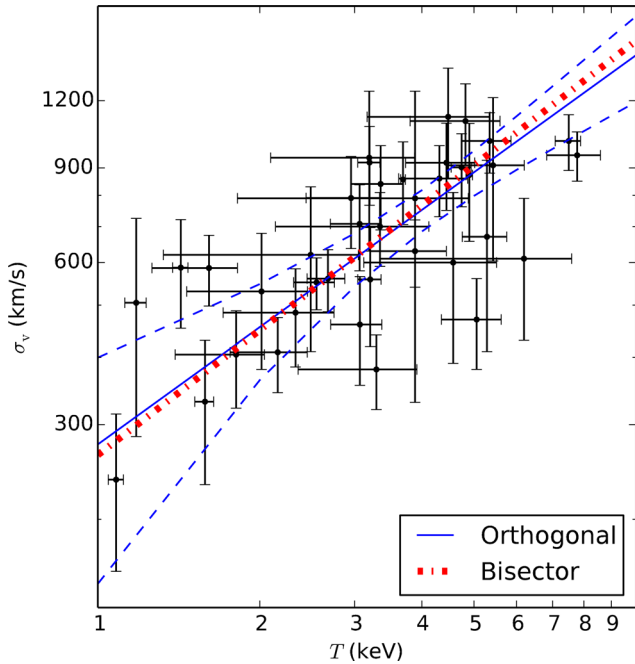


Figure 5. The σ_v - T relation assuming no evolution, i.e. $C = 0$ in equation (3), for the combined sample. All lines are as explained in Fig. 3.

straightforward, and is outside the scope of this paper, but for completeness we briefly discuss causes of bias identified in previous studies. Old, Gray & Pearce (2013) studied the recovery of velocity dispersions from simulation data and explored how sample selection can impact the measurements and cause a bias. They introduced I -band magnitude limits and found that the velocity dispersion recovered from the haloes was systematically higher than that from the galaxies. When this sample was further limited to just the brightest galaxies, this discrepancy was enhanced. They suggest that the rea-

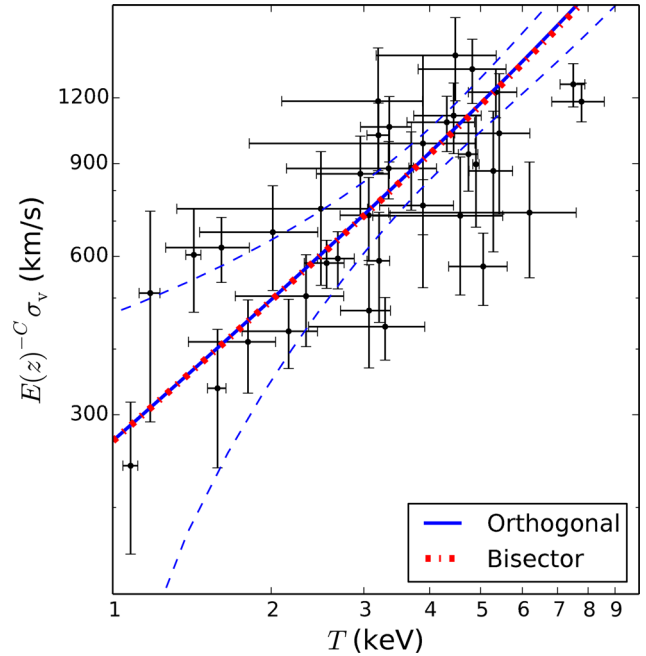


Figure 6. Plots showing the σ_v - T relation for the combined sample with varying evolution, i.e. C is a free parameter in equation (3). The velocity dispersion is scaled to take into account the evolution by multiplying by $E(z)^{-C}$. All lines are as explained in Fig. 3.

son for this is that dynamical friction greatly affects the velocity of the galaxies, and therefore to reduce this bias a strictly magnitude-limited sample should be avoided. Old et al. (2013) also calculated the velocity dispersion over different radial distances to see how it varied as a function of distance from the cluster centre. They found that the velocity dispersion was sensitive to the radius in which it was measured with a difference of 10 per cent in measurements being

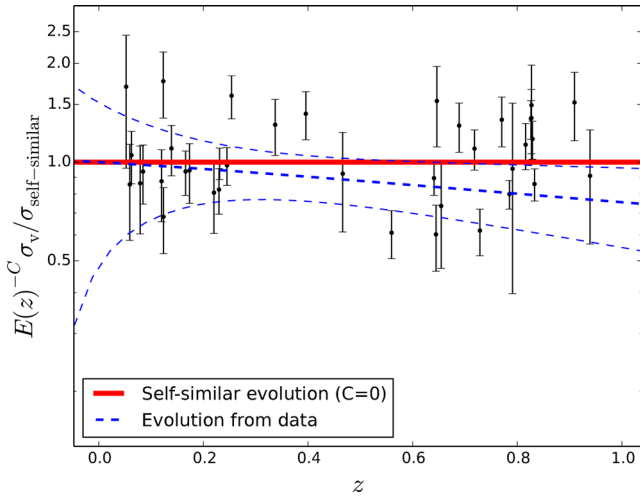


Figure 7. Plot showing the evolution of the normalization of the σ_v-T relation obtained for the data with the 95 percent confidence intervals in the dashed lines as compared to the self-similar relation which predicts no evolution shown as the solid line. The black points show our sample data.

found between 0.5 and $1 R_{200}$. Sifón et al. (2016) also studied the impact of the choice of radius on velocity dispersion measurements, and found that the bias is negligible for measurements that sample beyond $0.7 R_{200}$ (see their fig. 4). Since our observations sample out to at least $0.7 R_{200}$ for all clusters, and beyond R_{200} for more than

Table 7. Best-fitting values for the parameters in equation (4) (slope, intercept and scatter) for the various models obtained from simulations without evolution. For the Millennium Gas Project, we use dark matter (DM) and stars as the tracers for the velocity dispersion. The BAHAMAS simulation uses galaxies. The Millennium Gas simulations use spectroscopic-like temperatures (T_{sl}) and the BAHAMAS simulation use spectroscopic temperatures (T_s). Caldwell et al. (in preparation) present a different method for determining the σ_v-T relation as discussed in Section 5.2, the results of which are also shown below.

Simulation	σ_{tracer}	T_{model}	A	B	S
Millennium Gas	DM	T_{sl}	-0.011 ± 0.002	0.553 ± 0.008	0.028 ± 0.001
Millennium Gas	Stars	T_{sl}	-0.034 ± 0.003	0.621 ± 0.010	0.034 ± 0.001
BAHAMAS	Galaxies	T_s	-0.055 ± 0.003	0.848 ± 0.012	0.055 ± 0.001
BAHAMAS (Caldwell et al. in preparation)	Galaxies	T_s	-0.133	0.545	

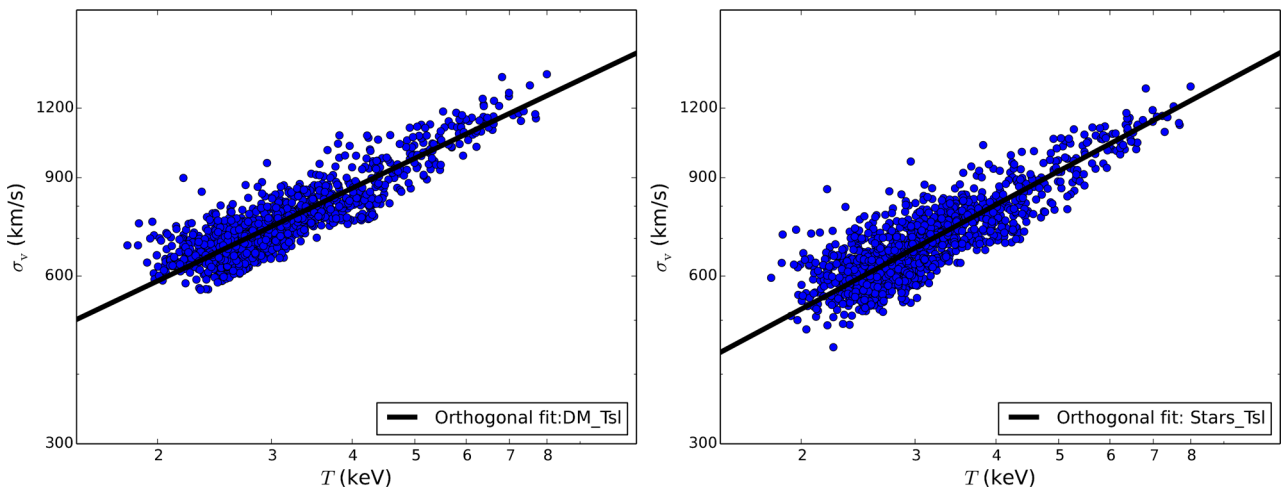


Figure 8. The σ_v-T relation for the Millennium Gas Project simulations using dark matter and stars as proxies for the velocity dispersion. The blue dots are the data obtained from the simulation and the solid black line shows the fit using the orthogonal regression method. The slope is slightly steeper for the stars ($B = 0.62 \pm 0.01$) than for the dark matter ($B = 0.55 \pm 0.08$) but both are consistent with previous studies of the σ_v-T relation and the results obtained from our data.

half the sample, we expect our velocity dispersion measurements to be unaffected by this source of bias. We used these two sets of simulations to test our orthogonal fitting methods both with and without evolution.

5.3 Comparison with simulations - fitting with no evolution

The orthogonal fitting method described in Section 3.2 was applied to both sets of simulations with $C = 0$. The parameters A , B and S for both the Millennium Gas Project and BAHAMAS simulations are shown in Table 7. The σ_v-T relation for the Millennium Gas Project with the two different σ_v proxies are shown in Fig. 8. The slope is slightly steeper for the stars ($B = 0.62 \pm 0.01$) than for the dark matter ($B = 0.55 \pm 0.08$) but both are consistent with previous studies of the σ_v-T relation and the results obtained from our data. Fig. 9 shows that the orthogonal fit to the full BAHAMAS sample systematically overestimates the average velocity dispersion at $T > 5$ keV. This may be due, in part, to the model not being a complete description of the data, as the scatter appears to vary with temperature. This is not captured in our orthogonal regression model (equation 4), i.e. S is assumed to be constant with both T and z . A comparison was made to a fit performed by Caldwell et al. (in preparation) to the BAHAMAS data. In this method the σ^2-kT relation was derived by first parametrically determining the mean functions and redshift evolution of velocity dispersion and temperature, separately, with respect to mass (M_{500} critical). The velocity dispersion measurements are averaged in $0.25 \log_{10}(M_{500c})$ mass

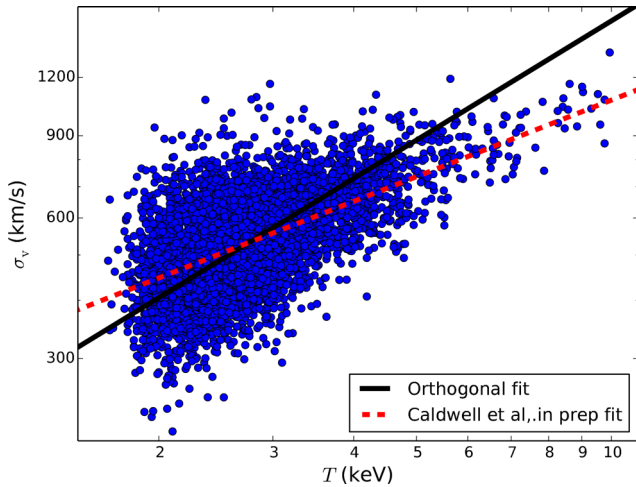


Figure 9. Plot showing the σ_v – T relation for the BAHAMAS simulation data. The blue circles represent the data points from the simulation. The solid line is the fit obtained using the orthogonal method and the dashed line is the fit obtained using the method described in Section 5.2 and performed by Caldwell et al. (in preparation). From this it can be seen that the orthogonal fit overestimates the velocity dispersion at $T_X > 5$ keV (see Section 5.2).

bins, to avoid biases from high cluster counts and the large scatter seen at low T (Fig. 9). These mean values of velocity dispersion and mass are fit with a power law, and the temperature relation is derived with the same method. This was converted into the σ_v – T relation (with slope $B = 0.545$) that is plotted in Fig. 9. This method provides a better fit to BAHAMAS data over the full temperature range than the orthogonal method. We use the slope obtained using the Caldwell et al. method for further studies and comparisons. We examine the effect of bias in the recovered slope on our results in Section 5.4. We note that there is no single method which gives the underlying ‘true’ scaling relation in the presence of errors on both variables and intrinsic scatter: the recovered slope and normalization depend upon the details of the method used. The fitting of a scaling relation is also affected by the selection processes used when determining your sample and for this study this has not been corrected for. Since our clusters are selected on X-ray luminosity rather than temperature or velocity dispersion we believe that our values are not biased and therefore selection effects will not have as big an impact on our results.

5.4 The effect of biased slope measurements on the evolution of the normalization

Having seen, using the BAHAMAS simulation, that the slope recovered using the orthogonal regression method may be biased high, we now discuss the potential impact of a biased slope measurement on our conclusions regarding the observed cluster sample in Section 5.1.

To investigate this, we generated 1000 mock samples (each containing 38 clusters) from the BAHAMAS simulation with the same temperature distribution as the observed sample, and applied the orthogonal regression method. Fig. 10 shows the distribution of the recovered slope values. The average is $B = 0.69 \pm 0.13$, which is 2σ higher than the slope obtained from the fit performed by Caldwell et al. (in preparation, Section 5.2). Therefore, if the BAHAMAS sample is representative of the real cluster population, then we would conclude that the slope we have measured for the observed cluster sample is biased high. To check if a biased slope estimate

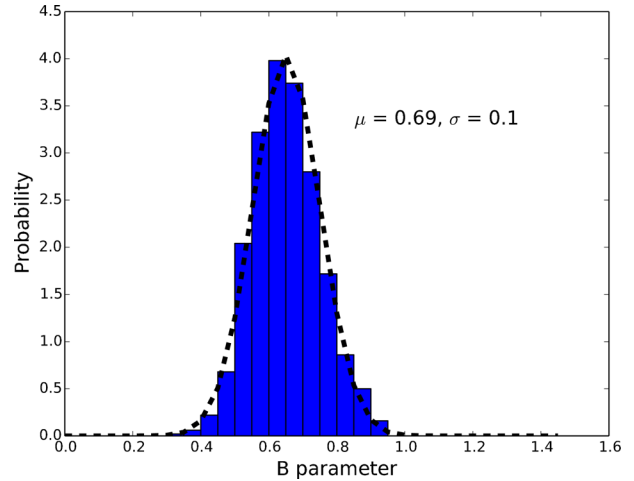


Figure 10. This histogram shows the probability of getting a specific value for the slope of the best-fitting σ – T relation given a set T distribution. We chose various subsamples from the BAHAMAS simulation which had the same T distribution as our sample and calculated the slope for each. The mean slope obtained is $B = 0.69 \pm 0.13$, which is within 2σ of the value obtained from Caldwell et al (in preparation), so there is a slight bias from the distribution of the sample.

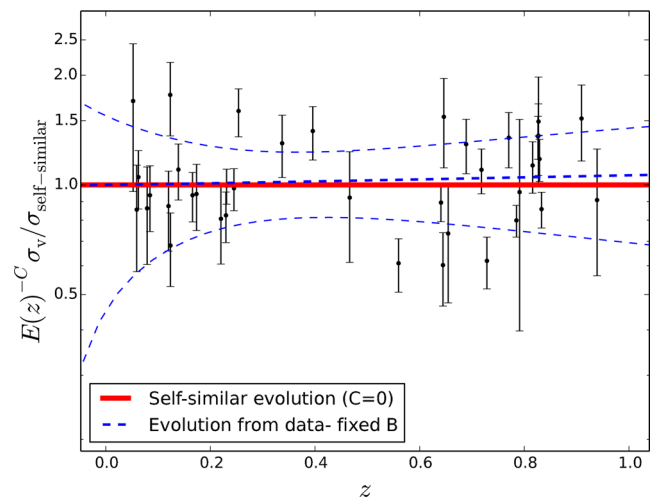


Figure 11. Plot showing the evolution of the normalization of the σ_v – T relation, with $B = 0.545$, obtained for the observed cluster sample with the 95 per cent confidence intervals in the dashed lines, as compared to the self-similar relation which predicts no evolution shown as the solid line. The black points show the measurements for the clusters in our sample.

affects our conclusions regarding the lack of significant evidence for evolution of the normalization of the relation (Section 4.2), we fixed the slope to $B = 0.545$ and re-ran the orthogonal fit for the observed cluster sample. We found $C = 0.15 \pm 0.28$, which is consistent with no evolution (Fig. 11). Therefore, even if the slope value of $B = 0.86 \pm 0.14$ that we measured was biased high for any reason, this does not affect our conclusion that we do not see significant evidence in favour of evolution.

5.5 Comparison with simulations – fitting with evolution

We now investigate evolution in the normalization of the σ_v – T relation in the simulations by fitting for the value of C , as we did for the observed sample (see Section 4.2). The results are shown

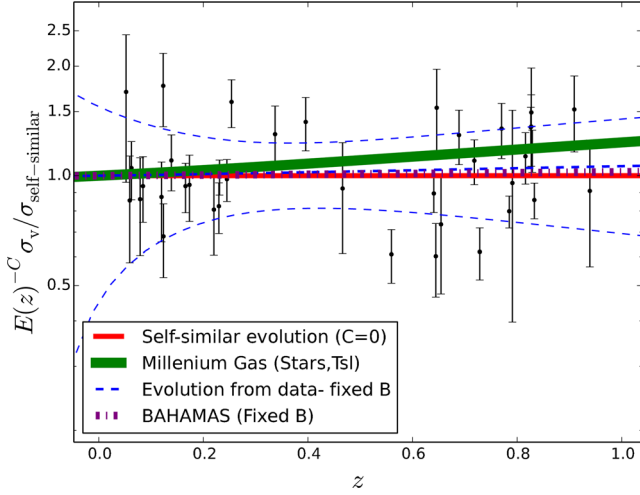


Figure 12. We compared the evolution of the normalization of σ_v-T relation of the Millennium Gas and BAHAMAS simulations with the self-similar relation and that found from our data using a fixed slope. The solid line shows the line representing the self-similar relation i.e. $C = 0$, the dot-dashed line represents the BAHAMAS simulation results with a fixed $B = 0.545$ to avoid bias and the vertically dashed line represents the result from the Millennium Gas simulation. The blue dashed line and black points are our orthogonal fit and observed sample, respectively.

in Table 8 and graphically in Fig. 12. The BAHAMAS simulation was tested both with a slope that was allowed to vary and a fixed slope. Although, in Section 5.4 we showed that the overestimated slope does not affect evolution, we included a fixed slope for further comparison. Both were found to be consistent with zero evolution, further proving that the biased slope does not affect evolution. However, the simulations from the Millennium Gas Project show small but significant positive evolution ($C = 0.273 \pm 0.013$ for σ_{Stars} and T_{sl}). To see the reason for this, we can re-write the σ_v-T relation in terms of the σ_v-M and $T-M$ relations, where M is the cluster mass (see e.g. Maughan 2014). We define

$$\sigma_v = 10^{A_{\sigma_v T}} \left(\frac{T}{5 \text{ keV}} \right)^{B_{\sigma_v T}} E(z)^{C_{\sigma_v T}}, \quad (9)$$

where

$$B_{\sigma_v T} = B_{\sigma_v M} / B_{TM},$$

$$A_{\sigma_v T} = A_{\sigma_v M} - A_{TM} B_{\sigma_v T},$$

and

$$C_{\sigma_v T} = C_{\sigma_v M} - C_{TM} B_{\sigma_v T}. \quad (10)$$

Here, A , B and C have the same meaning as before, and the subscripts indicate the corresponding relation (e.g. B_{TM} indicates the slope of the $T-M$ relation). If we set $C_{\sigma_v M} = 1/3$, $C_{TM} = 2/3$ and $B_{\sigma_v T} = 1/2$ as predicted by the self-similar relation, then we obtain $C_{\sigma_v T} = 0$ as expected. We performed fits to determine the values of $C_{\sigma_v M}$,

C_{TM} and $B_{\sigma_v T}$ in the Millennium Gas simulation at $z = 0$ and 0.5. We found that $C_{\sigma_v M} = 1/3$ when using either σ_{Stars} or σ_{DM} as the measure of σ_v , and that $B_{\sigma_v T}$ varied from 0.55 to 0.6 (depending on whether spectroscopic-like or mass-weighted temperature estimates were used), which is slightly higher than the self-similar value, but not by enough to explain the positive evolution measured in the σ_v-T relation. This leads to the conclusion that the evolution is driven by the value of C_{TM} , and it was found that the measured value for the dark matter was $C_{TM} = 2/3$ as expected, but that this decreased to values between 0 and 0.2 for the gas. Therefore in the Millennium Gas simulation, the lack of redshift evolution in the $T-M$ relation drives the positive evolution in the σ_v-T relation. The most likely explanation for the lack of redshift evolution in the $T-M$ relation in the Millennium Gas simulation is the absence of radiative cooling. When both cooling and feedback are included in simulations (as in BAHAMAS), the feedback acts as a regulation mechanism, heating the surrounding dense gas and expelling it from the cluster core. This in turn leads to higher entropy gas flowing inwards. In the Millennium Gas simulation, the feedback model heats the gas and directly increases its entropy, which is eventually distributed throughout the cluster. This builds up over time as more and more energy is pumped into the gas from the growing black holes, and has the effect of slowing down the evolution of the $T-M$ relation (compared to the evolution expected due to the decreasing background density with redshift). This in turn leads to the positive evolution of the σ_v-T relation. It is likely that the more sophisticated feedback model used in BAHAMAS, where the entropy evolution is driven by radiative cooling, is the more realistic of the two.

6 CONCLUSIONS

We have studied the evolution of the velocity dispersion-temperature (σ_v-T) relation using a cluster sample spanning the range $0.0 < z < 1.0$ drawn from XCS. This work improves upon previous studies in terms of the use of a homogeneous cluster sample and the number of $z > 0.5$ clusters included. We present new redshift and velocity dispersion measurements based on Gemini data for 12 such $z > 0.5$ XCS clusters. We used an orthogonal regression method to measure the normalization, slope and intrinsic scatter of the σ_v-T relation for two subsamples: 19 clusters at $z < 0.5$, and 19 clusters with $z > 0.5$. In both cases, we found the slope of the relation to be consistent with the findings of previous studies, i.e. slightly steeper than expected from self-similarity. Under the assumption that the slope of the relation does not evolve with redshift, we measured the evolution of the normalization of the relation using the complete sample of 38 clusters. We found this to be slightly negative but not significantly different from the self-similar solution ($\sigma_v \propto T^{0.86 \pm 0.14} E(z)^{-0.37 \pm 0.33}$). Moreover, a no evolution model is the preferred choice when considering the AIC. We applied the same scaling relation analysis methods to the BAHAMAS and Millennium Gas cosmological hydrodynamical simulations. The σ_v-T relation does not evolve in BAHAMAS, in agreement with our

Table 8. Best-fitting values for the parameters in equation (4) (slope, intercept, scatter and evolution) for the various models obtained from simulations. All abbreviations are as in Table 7.

Simulation	σ_{tracer}	T_{model}	A	B	S	C
Millennium Gas	DM	T_{sl}	-0.031 ± 0.002	0.551 ± 0.006	0.0220 ± 0.0010	0.371 ± 0.014
Millennium Gas	Stars	T_{sl}	-0.056 ± 0.002	0.619 ± 0.009	0.0295 ± 0.0010	0.397 ± 0.019
BAHAMAS (fixed B)	Galaxies	T_{s}	-0.135 ± 0.002	0.545	0.0390 ± 0.0010	0.046 ± 0.016
BAHAMAS (varying B)	Galaxies	T_{s}	-0.071 ± 0.005	0.779 ± 0.014	0.0570 ± 0.0010	-0.029 ± 0.024

findings for the observed cluster sample. However, positive evolution is seen in the Millennium Gas simulation. The difference is most likely due to the inclusion of self-consistent modelling of radiative cooling in BAHAMAS, which is absent in the Millennium Gas simulation. This leads to a very slowly evolving T – M relation in the Millennium Gas simulation, which in turn drives the positive evolution of the σ_v – T relation. While this work has improved upon previous studies in terms of the number of high-redshift clusters included, we note that the uncertainties on the scaling relation parameters are still rather large, and a combination of better measurements of individual cluster properties and a larger sample are required to make further progress. Future studies will look at implementing the Bayesian method described by Kelly (2007) to account for intrinsic scatter and measurement errors and looking at possible selection effects.

ACKNOWLEDGEMENTS

SW and MH acknowledge financial support from the National Research Foundation and SKA South Africa. This research has made use of the NASA/IPAC Extragalactic Database (NED) which is operated by the Jet Propulsion Laboratory, California Institute of Technology, under contract with the National Aeronautics and Space Administration. Based on observations obtained at the Gemini Observatory, which is operated by the Association of Universities for Research in Astronomy, Inc., under a cooperative agreement with the NSF on behalf of the Gemini partnership: the National Science Foundation (United States), the National Research Council (Canada), CONICYT (Chile), the Australian Research Council (Australia), Ministério da Ciência, Tecnologia e Inovação (Brazil) and Ministerio de Ciencia, Tecnología e Innovación Productiva (Argentina). PAT acknowledges support from the Science and Technology Facilities Council (grant number ST/L000652/1). JPS gratefully acknowledges support from a Hintze Research Fellowship. STK acknowledges support from STFC (grant number ST/L000768/1).

REFERENCES

- Abazajian K. N. et al., 2009, *ApJS*, 182, 543
 Adami C. et al., 2011, *A&A*, 526, A18
 Arnaud M., Pointecouteau E., Pratt G. W., 2005, *A&A*, 441, 893
 Basilakos S., Plionis M., Georgakakis A., Georgantopoulos I., Gaga T., Kolokotronis V., Stewart G. C., 2004, *MNRAS*, 351, 989
 Beers T. C., Flynn K., Gebhardt K., 1990, *AJ*, 100, 32
 Bellagamba F., Maturi M., Hamana T., Meneghetti M., Miyazaki S., Moscardini L., 2011, *MNRAS*, 413, 1145
 Bird C. M., Mushotzky R. F., Metzler C. A., 1995, *ApJ*, 453, 40
 Bower R. G., 1997, *MNRAS*, 288, 355
 Bower R. G., McCarthy I. G., Benson A. J., 2008, *MNRAS*, 390, 1399
 Branchesi M., Gioia I. M., Fanti C., Fanti R., 2007, *A&A*, 472, 739
 Bryan G. L., Norman M. L., 1998, *ApJ*, 495, 80
 Burenin R. A., Vikhlinin A., Hornstrup A., Ebeling H., Quintana H., Mescheryakov A., 2007, *ApJS*, 172, 561
 Burnham K. P., Anderson D. R., 2002, *Model Selection and Multimodel Inference: A Practical Information-Theoretic Approach*, 2 edn. Springer-Verlag, New York
 Cappi A., Held E. V., Marano B., 1998, *A&AS*, 129, 31
 Cash W., 1979, *ApJ*, 228, 939
 Clerc N., Sadibekova T., Pierre M., Pacaud F., Le Fèvre J.-P., Adami C., Altieri B., Valtchanov I., 2012, *MNRAS*, 423, 3561
 Clerc N. et al., 2014, *MNRAS*, 444, 2723
 Cohn J. D., White M., 2005, *Astropart. Phys.*, 24, 316
 Collins C. A. et al., 2009, *Nature*, 458, 603
 Crawford S. M., Wirth G. D., Bershadsky M. A., 2014, *ApJ*, 786, 30
 De Lucia G., Blaizot J., 2007, *MNRAS*, 375, 2
 De Propris R. et al., 2002, *MNRAS*, 329, 87
 Dickey J. M., 1990, in Thronson H. A., Jr, Shull J. M., eds, *Astrophysics and Space Science Library* Vol. 161, *The Interstellar Medium in Galaxies*. Kluwer, Dordrecht, p. 473
 Donahue M., Voit G. M., Scharf C. A., Gioia I. M., Mullis C. R., Hughes J. P., Stocke J. T., 1999, *ApJ*, 527, 525
 Edge A. C., Stewart G. C., 1991, *MNRAS*, 252, 428
 Ettori S., Tozzi P., Borgani S., Rosati P., 2004, *A&A*, 417, 13
 Fadda D., Girardi M., Giuricin G., Mardirossian F., Mezzetti M., 1996, *ApJ*, 473, 670
 Fassbender R. et al., 2011, *New J. Phys.*, 13, 125014
 Finn R. A. et al., 2005, *ApJ*, 630, 206
 Finoguenov A. et al., 2007, *ApJS*, 172, 182
 Gioia I. M., Luppino G. A., 1994, *ApJS*, 94, 583
 Gioia I. M., Wolter A., Mullis C. R., Henry J. P., Böhringer H., Briel U. G., 2004, *A&A*, 428, 867
 Girardi M., Fadda D., Giuricin G., Mardirossian F., Mezzetti M., Biviano A., 1996, *ApJ*, 457, 61
 Glazebrook K., Bland-Hawthorn J., 2001, *PASP*, 113, 197
 Hao J. et al., 2010, *ApJS*, 191, 254
 Hasselfield M. et al., 2013, *J. Cosmol. Astropart. Phys.*, 7, 8
 Hennawi J. F. et al., 2008, *AJ*, 135, 664
 Hilton M. et al., 2009, *ApJ*, 697, 436
 Hilton M. et al., 2010, *ApJ*, 718, 133
 Hilton M. et al., 2012, *MNRAS*, 424, 2086
 Hoekstra H., Herbonnet R., Muzzin A., Babul A., Mahdavi A., Viola M., Cacciato M., 2015, *MNRAS*, 449, 685
 Hogg D. W., Bovy J., Lang D., 2010, preprint ([arXiv:1008.4686](https://arxiv.org/abs/1008.4686))
 Kaiser N., 1986, *MNRAS*, 222, 323
 Kay S. T., da Silva A. C., Aghanim N., Blanchard A., Liddle A. R., Puget J.-L., Sadat R., Thomas P. A., 2007, *MNRAS*, 377, 317
 Kelly B. C., 2007, *ApJ*, 665, 1489
 Koester B. P. et al., 2007, *ApJ*, 660, 239
 Kravtsov A. V., Borgani S., 2012, *ARA&A*, 50, 353
 Kurtz M. J., Mink D. J., 1998, *PASP*, 110, 934
 Le Brun A. M. C., McCarthy I. G., Schaye J., Ponman T. J., 2014, *MNRAS*, 441, 1270
 Lloyd-Davies E. J. et al., 2011, *MNRAS*, 418, 14
 Lubin L. M., Bahcall N. A., 1993, *ApJ*, 415, L17
 Lumb D. H. et al., 2004, *A&A*, 420, 853
 Magnelli B., Elbaz D., Chary R. R., Dickinson M., Le Borgne D., Frayer D. T., Willmer C. N. A., 2009, *A&A*, 496, 57
 Mann A. W., Ebeling H., 2012, *MNRAS*, 420, 2120
 Maughan B. J., 2014, *MNRAS*, 437, 1171
 Maughan B. J., Jones L. R., Ebeling H., Scharf C., 2006, *MNRAS*, 365, 509
 Maughan B. J., Giles P. A., Randall S. W., Jones C., Forman W. R., 2012, *MNRAS*, 421, 1583
 Mazzotta P., Rasia E., Moscardini L., Tormen G., 2004, *MNRAS*, 354, 10
 McCarthy I. G., Schaye J., Bird S., Le Brun A. M. C., 2016, *MNRAS*, preprint ([arXiv:1603.02702](https://arxiv.org/abs/1603.02702))
 Mehrrens N. et al., 2012, *MNRAS*, 423, 1024
 Mewe R., Schrijver C. J., 1986, *A&A*, 169, 178
 Mulchaey J. S., Lubin L. M., Fassnacht C., Rosati P., Jeltama T. E., 2006, *ApJ*, 646, 133
 Mullis C. R. et al., 2003, *ApJ*, 594, 154
 Nastasi A. et al., 2014, *A&A*, 564, A17
 Old L., Gray M. E., Pearce F. R., 2013, *MNRAS*, 434, 2606
 Ortiz-Gil A., Guzzo L., Schuecker P., Böhringer H., Collins C. A., 2004, *MNRAS*, 348, 325
 Perlman E. S., Horner D. J., Jones L. R., Scharf C. A., Ebeling H., Wegner G., Malkan M., 2002, *ApJS*, 140, 265
 Planck Collaboration XVI, 2014, *A&A*, 571, A16
 Planck Collaboration XXIV, 2015, preprint ([arXiv:1502.01597](https://arxiv.org/abs/1502.01597))
 Ponman T. J., Bourner P. D. J., Ebeling H., Böhringer H., 1996, *MNRAS*, 283, 690
 Poole G. B., Babul A., McCarthy I. G., Fardal M. A., Bildfell C. J., Quinn T., Mahdavi A., 2007, *MNRAS*, 380, 437

- Quintana H., Melnick J., 1982, *AJ*, 87, 972
 Randall S. W., Sarazin C. L., Ricker P. M., 2002, *ApJ*, 577, 579
 Reichardt C. L. et al., 2013, *ApJ*, 763, 127
 Ritchie B. W., Thomas P. A., 2002, *MNRAS*, 329, 675
 Rozo E. et al., 2009, *ApJ*, 699, 768
 Sahlén M. et al., 2009, *MNRAS*, 397, 577
 Sakelliou I., Merrifield M. R., 1998, *MNRAS*, 293, 489
 Schafer R. A., 1991, *XSPEC*, An X-ray Spectral Fitting Package: Version 2 of the User's Guide. European Space Agency, Paris
 Scharf C. A., Ebeling H., Perlman E., Malkan M., Wegner G., 1997, *ApJ*, 477, 79
 Short C. J., Thomas P. A., Young O. E., Pearce F. R., Jenkins A., Muanwong O., 2010, *MNRAS*, 408, 2213
 Sifón C. et al., 2013, *ApJ*, 772, 25
 Sifón C. et al., 2016, *MNRAS*, 461, 248
 Silverman J. D. et al., 2005, *ApJ*, 618, 123
 Springel V. et al., 2005, *Nature*, 435, 629
 Stott J. P. et al., 2010, *ApJ*, 718, 23
 Struble M. F., Rood H. J., 1999, *ApJS*, 125, 35
 Šuhada R. et al., 2011, *A&A*, 530, A110
 Takey A., Schwobe A., Lamer G., 2011, *A&A*, 534, A120
 Takey A., Schwobe A., Lamer G., 2013, *A&A*, 558, A75
 Tonry J., Davis M., 1979, *AJ*, 84, 1511
 Tran K.-V. H., Kelson D. D., van Dokkum P., Franx M., Illingworth G. D., Magee D., 1999, *ApJ*, 522, 39
 Vikhlinin A., McNamara B. R., Forman W., Jones C., Quintana H., Hornstrup A., 1998, *ApJ*, 502, 558
 Vikhlinin A., van Speybroeck L., Markevitch M., Forman W. R., Grego L., 2002, *ApJ*, 578, L107
 Vikhlinin A., Kravtsov A., Forman W., Jones C., Markevitch M., Murray S. S., Van Speybroeck L., 2006, *ApJ*, 640, 691
 Vikhlinin A. et al., 2009, *ApJ*, 692, 1060
 Voit G. M., 2005, *Rev. Mod. Phys.*, 77, 207
 von der Linden A. et al., 2014, *MNRAS*, 439, 2
 White D. A., Jones C., Forman W., 1997, *MNRAS*, 292, 419
 Wu X.-P., Fang L.-Z., Xu W., 1998, *A&A*, 338, 813
 Wu X.-P., Xue Y.-J., Fang L.-Z., 1999, *ApJ*, 524, 22
 Xue Y.-J., Wu X.-P., 2000, *ApJ*, 538, 65
 Yoon J. H., Schawinski K., Sheen Y.-K., Ree C. H., Yi S. K., 2008, *ApJS*, 176, 414

SUPPORTING INFORMATION

Additional Supporting Information may be found in the online version of this article:

APPENDIX B. REDSHIFT CATALOGUE.

APPENDIX C. VELOCITY HISTOGRAMS.

(<http://www.mnras.oxfordjournals.org/lookup/suppl/doi:10.1093/mnras/stw1947/-/DC1>).

Please note: Oxford University Press is not responsible for the content or functionality of any supporting materials supplied by the authors. Any queries (other than missing material) should be directed to the corresponding author for the article.

APPENDIX A: OBSERVATIONS LOG**Table A1.** Spectroscopic observations log. For all observations the R400 grating and the OG515 filter was used.

Cluster Name	Mask	Slits	Airmass range	Observation date	Frames(s)	Seeing (arcsec)
XMMXCS J005656.6–274031.9	GS-2012B-Q-011-03	33	1.22	2012-10-19	1 × 1830	
"	"		1.48–1.76	2012-10-16	2 × 1830	
"	"		1.01–1.04	2012-10-15	3 × 1830	0.76–0.80
"	GS-2012B-Q-011-04	35	1.05–1.35	2012-11-14	4 × 1830	
XMMXCS J015241.1–133855.9	GS-2011B-Q-050-01	33	1.05–1.21	2011-12-02	6 × 1830	
"	GS-2011B-Q-050-02	34	1.05–1.65	2011-12-03	6 × 1830	
XMMXCS J021734.7–051326.9	GS-2012B-Q-011-06	34	1.14–1.48	2012-12-05	4 × 1830	
XMMXCS J025006.4–310400.8	GS-2012B-Q-011-09	32	1.11–1.20	2012-11-24	2 × 1830	
"	"		1.01–1.19	2012-11-21	4 × 1830	
"	GS-2010B-Q-046-06	35	1.06–1.12	2010-11-14	2 × 1830	0.50–0.60
"	"		1.06–1.44	2010-11-13	5 × 1830, 1 × 762	1
XMMXCS J030205.1–000003.6	GS-2011B-Q-050-03	32	1.17	2011-12-01	1 × 1830	
"	"		1.18	2011-11-20	1 × 1098	
"	"		1.17–1.45	2011-11-18	4 × 1830	
"	GS-2011B-Q-050-04	32	1.32	2011-12-31	1 × 1098	
"	"		1.23–1.74	2011-12-30	4 × 1830	0.85–1.40
"	GS-2011B-Q-050-05	33	1.27–1.57	2012-01-17	2 × 1830	0.7
XMMXCS J095940.7+023113.4	GS-2010B-Q-046-02	35	1.19–1.23	2011-01-09	3 × 1830	
"	"		1.19–1.25	2011-01-08	4 × 1830	
"	GS-2012A-Q-46-01	35	1.19–1.29	2012-03-18	4 × 1830	
"	"		1.19–1.23	2012-03-02	2 × 1830	
"	GS-2012A-Q-46-02	34	1.20–1.35	2012-03-27	3 × 1830	
"	"		1.23–1.46	2012-03-23	3 × 1830	0.8
"	GS-2012A-Q-46-03	34	1.21–1.54	2012-03-22	6 × 1830	0.65–0.70
XMMXCS J112349.3+052956.8	GS-2012A-Q-46-05	33	1.23–1.33	2012-04-22	5 × 1830	
"	"		1.47	2012-04-21	1 × 1830	
"	GS-2012A-Q-46-06	32	1.25–1.65	2012-05-15	4 × 1830	0.63–0.76
"	"		1.45–1.66	2012-04-22	2 × 1830	
"	GS-2010B-Q-046-03	33	1.26	2011-01-31	1 × 1830	
"	"		1.35–1.64	2011-01-29	2 × 1525, 1 × 975	
"	"		1.23–1.24	2011-01-27	2 × 1830	
XMMXCS J113602.9–032943.2	GS-2012A-Q-46-07	36	1.14	2012-05-24	1 × 1830	
"	"		1.12	2012-05-23	1 × 1830	
"	"		1.12–1.16	2012-05-20	3 × 1830	
"	"		1.12	2012-05-19	1 × 1830	
"	GS-2012A-Q-46-08	33	1.48–1.76	2012-07-15	2 × 1830	
"	"		1.41–1.80	2012-07-11	3 × 1830	0.50–0.70
"	"		1.5	2012-07-10	1 × 1830	
XMMXCS J134305.1–000056.8	GS-2012A-Q-46-10	36	1.16–1.23	2012-05-24	4 × 1830	
"	"		1.24	2012-05-21	1 × 1830	
"	GS-2012A-Q-46-11	34	1.25	2012-07-10	1 × 1830	
"	"		1.16–1.19	2012-07-09	2 × 1830	
"	"		1.2	2012-07-06	1 × 1830	
"	"		1.54–1.84	2012-06-22	2 × 1830	
XMMXCS J145009.3+090428.8	GN2012A-Q-070-05	32	1.02–1.05	2012-07-09	2 × 1800	1.15
"	"		1.11–1.62	2012-06-26	4 × 1800	0.84–0.98
"	GN2012A-Q-070-06	34	1.02–1.04	2012-07-07	2 × 1800	
"	"		1.09–1.17	2012-07-06	2 × 1800	
"	"		1.48–1.79	2012-06-27	2 × 1800	
"	GN2012A-Q-070-07	33	1.22–1.59	2012-07-22	3 × 1800	
"	"		1.04–1.16	2012-07-08	3 × 1800	1
XMMXCS J215221.0–273022.6	GS-2010B-Q-046-04	36	1.14–1.24	2010-11-12	2 × 1830	
"	"		1.02–1.21	2010-09-14	4 × 1830	
"	GS-2011B-Q-050-06	34	1.07–1.15	2011-10-05	2 × 1830	
"	"		1.12–1.56	2011-09-18	4 × 1830	0.60–1.00
"	GS-2011B-Q-050-07	34	1.00–1.10	2011-10-24	4 × 1830	
"	"		1.05–1.12	2011-10-16	2 × 1830	
XMMXCS J230247.7+084355.9	GN2012A-Q-070-10	34	1.37	2012-08-08	1 × 1800	0.60–0.68
"	"		1.02–1.11	2012-07-30	5 × 1800	0.43–0.86
"	GN2012A-Q-070-11	33	1.18–1.31	2012-08-13	2 × 1800	
"	"		1.02–1.08	2012-08-09	3 × 1800	0.60–0.68
"	"		1.19	2012-08-08	1 × 1800	1

This paper has been typeset from a \LaTeX file prepared by the author.